The Mesoscale and Microscale Structure and Organization of Clouds and Precipitation in Midlatitude Cyclones. I: A Case Study of a Cold Front[1]

PETER V. HOBBS, THOMAS J. MATEJKA, PAUL H. HERZEGH,[2]
JOHN D. LOCATELLI AND ROBERT A. HOUZE, JR.

Atmospheric Sciences Department, University of Washington, Seattle 98195

(Manuscript received 25 May 1979, in final form 9 October 1979)

ABSTRACT

Detailed information is deduced on the mesoscale organization of precipitation, the structures of the clouds, the air flows associated with mesoscale rainbands, and the precipitation efficiencies and the mechanisms producing precipitation in the rainbands associated with a cold front. Measurements were obtained with quantitative reflectivity and Doppler radars, two instrumented aircraft, serial rawinsondes and a network of ground stations.

The regions of heaviest precipitation were organized into a complex mesoscale rainband in the warm-sector air ahead of the front, a narrow band of precipitation at the surface cold front, and four wide cold-frontal rainbands. The wide cold-frontal rainbands and the smaller mesoscale areas of precipitation within them moved with the velocities of the winds between ~3–6 km. The narrow rainband, which was produced by strong convergence and convection in the boundary layer, moved with the speed of the cold front at the surface. A coupled updraft and downdraft was probably responsible for the heavy precipitation on the cold front being organized, on the small mesoscale, into ellipsoidal areas with similar orientations.

The precipitation efficiencies in the warm-sector and narrow cold-frontal rainbands were ~40–50% and ~30–50%, respectively. One of the wide cold-frontal rainbands, in which there was a steady production of ice particles in the main updraft, had a precipitation efficiency of at least 80%, whereas another wide cold-frontal band, in which some precipitation evaporated before reaching the surface, had a precipitation efficiency of ~20%.

Ice particles from shallow convective cells aloft played important roles in the production of precipitation in the wide cold-frontal rainbands and in some regions of the warm-sector rainband. These "seed" ice particles grew by aggregation and by the deposition of vapor as they fell through lower level "feeder" clouds. About 20% of the mass of the precipitation reaching the ground in the wide cold-frontal rainbands originated in the upper level "seeder" zones and ~80% in the "feeder" zones.

1. Introduction

In recent years, there has been growing awareness that the key to significant progress in understanding precipitation processes and in improving the forecasting of precipitation lies in increasing our knowledge of mesoscale phenomena and their interactions with larger (i.e., synoptic) and smaller (i.e., convective and microphysical) scales. Extratropical cyclones, which dominate the weather and precipitation in temperate latitudes, are characterized by air motions, clouds and precipitation that are organized, often markedly so, on all these scales.

Several investigators (e.g., Nagle and Serebreny, 1962; Kreitzberg, 1964; Elliott and Hovind, 1964; Browning and Harrold, 1969; Austin and Houze, 1972) have studied and related aspects of the synoptic and subsynoptic scales of organization in extratropical cyclones. However, prior to 1973 there had not been a systematic and sustained attempt to investigate simultaneously the meso- and microscale phenomena in these systems which act in combination with larger scale processes to produce clouds and precipitation. In 1973 the Cloud Physics Group at the University of Washington (UW) initiated such a study and termed it the CYCLES (for CYCLonic Extratropical Storms) PROJECT.

Results of earlier analyses of CYCLES data, based predominantly on measurements collected in cyclonic storms as they passed across western Washington, have been reported by Hobbs *et al.* (1975), Houze *et al.* (1976a,b), Hobbs and Locatelli (1978), Hobbs (1978) and Matejka *et al.* (1979). The present paper, which describes a detailed case study of a cold front, is the first in a series in which significant use is made of later data collected in cyclones over the Pacific Ocean, before their landfall in Washington. In this study, three types of mesoscale rainbands preceding and accompanying a

---

[1] Contribution No. 506, Atmospheric Sciences Department, University of Washington.

[2] Present affiliation: The Center for the Environment and Man, Inc., Hartford, CT 06120.

0022-4928/80/030568-29$11.25

TABLE 1. Observational facilities used in the CYCLES PROJECT for investigating various scales of phenomena.

(a) Synoptic scale	(b) Mesoscale	(c) Microphysical scale
Visible and infrared photographs from satellites*	Radars (reflectivity and Doppler)	Two aircraft (UW B-23* and NCAR plane)
National Weather Service synoptic data*	Special network of ground stations for recording pressure, temperature and precipitation*	Vertically pointing Doppler radar
Rawinsondes	Two aircraft (UW B-23* and NCAR plane)	

* Data telemetered to CYCLES Control Center.

cold front are identified. Their horizontal and vertical structures and substructures are described, and the motions of the rainbands and of elements of their substructures are related to the larger scale wind field. Vertical air motions in the rainbands are computed from Doppler radar data and from aircraft measurements, and mesoscale airflows in the rainbands are deduced. The nature of the precipitation growth is examined, and the efficiencies of precipitation production in the rainbands are calculated. The description of this research begins in Section 3. In the following section, the field facilities available for the CYCLES PROJECT and the various ways in which they have been deployed and utilized are described. The information given in Section 2 is relevant not only to this paper but to subsequent papers in this series.

2. Facilities and their modes of operation in the CYCLES PROJECT

The first problem with which one is faced in attempting to describe synoptic, mesoscale and microscale processes in cyclonic storms is the vast range of spatial scales involved (~ 1 μm up to 10^3 km) and the need to document events which have time scales ranging from a few seconds to days. The facilities used in the CYCLES PROJECT to cover these scales are summarized in Table 1 and their disposition in the field is shown schematically in Fig. 1.

During CYCLES operations, many of the instruments in the field are monitored at a Control Center located at UW in Seattle, allowing decisions regarding the deployment of personnel and facilities to be made from this site. One person in each work shift is concerned with keeping abreast of the developing synoptic situation and providing short-term forecasts to the Project Director. National Weather Service (NWS) synoptic data are available through teleprinters and facsimile facilities at UW, and current SMS-2 satellite photographs are received every 30 min. In addition, extra high resolution satellite photographs of the project area are available for post-analyses.

There are 72 low-sensitivity raingages (resolution $\sim$0.25 mm of rainfall) in the project area which are operated by various governmental and local agencies. This network is supplemented by seven ground stations, each consisting of an automatic high-sensitivity tipping bucket raingage (resolution $\sim$0.04 mm per tip) and pressure and temperature sensors (Fig. 1). Data from these seven stations are transmitted to UW where they are displayed in real time on strip charts and digitized by computer.

Rawinsondes are launched at intervals ranging from 1 to 3 h during CYCLES operations. In 1973–74, 1974–75 and 1975–76 the rawinsonde unit was located at UW. In subsequent seasons it was moved to Pt. Brown on the Washington Coast (Fig. 1).

The characteristics of the three radars used in the project are listed in Table 2. During the 1974–75 field season, the CP-3 radar was located 14 km north of Seattle; in the following year it was located 45 km south of Seattle. Subsequently, it was moved to Pt. Brown. At Pt. Brown the radar can obtain an unobstructed view of storms over the Pacific Ocean out to a distance of $\sim$140 km from the coast (Fig. 1). Early in the CYCLES PROJECT it was discovered that the color display of Doppler velocities provided by the CP-3 radar could be used in real time to identify many important mesoscale features as well as frontal motions (Baynton *et al.*, 1977; Locatelli and Hobbs, 1978). Information from the CP-3 radar is relayed every 15 min by telephone or radio to the CYCLES Control Center.

The CP-3 radar is operated in three basic modes. The first is a PPI scanning mode designed to detect approaching storms. Once a storm has moved within a radar range and a decision has been made to study the storm, the CP-3 radar is operated in conjunction with the two research aircraft in either a Type 1 or a Type 2 mode.

In a Type 1 mode, the CP-3 is used to identify significant mesoscale features of the storm into which the aircraft are then directed. These mesoscale features are tracked by the radar and the aircraft as they move over the ocean and onto the land. In this type of operation, emphasis is placed on obtaining PPI's of reflectivity and Doppler velocities at different elevation angles, with occasional RHI scans through mesoscale features of particular interest and occasional vertically pointing radar measurements.

In the Type 2 mode, emphasis is placed on obtaining reflectivity and Doppler data at various

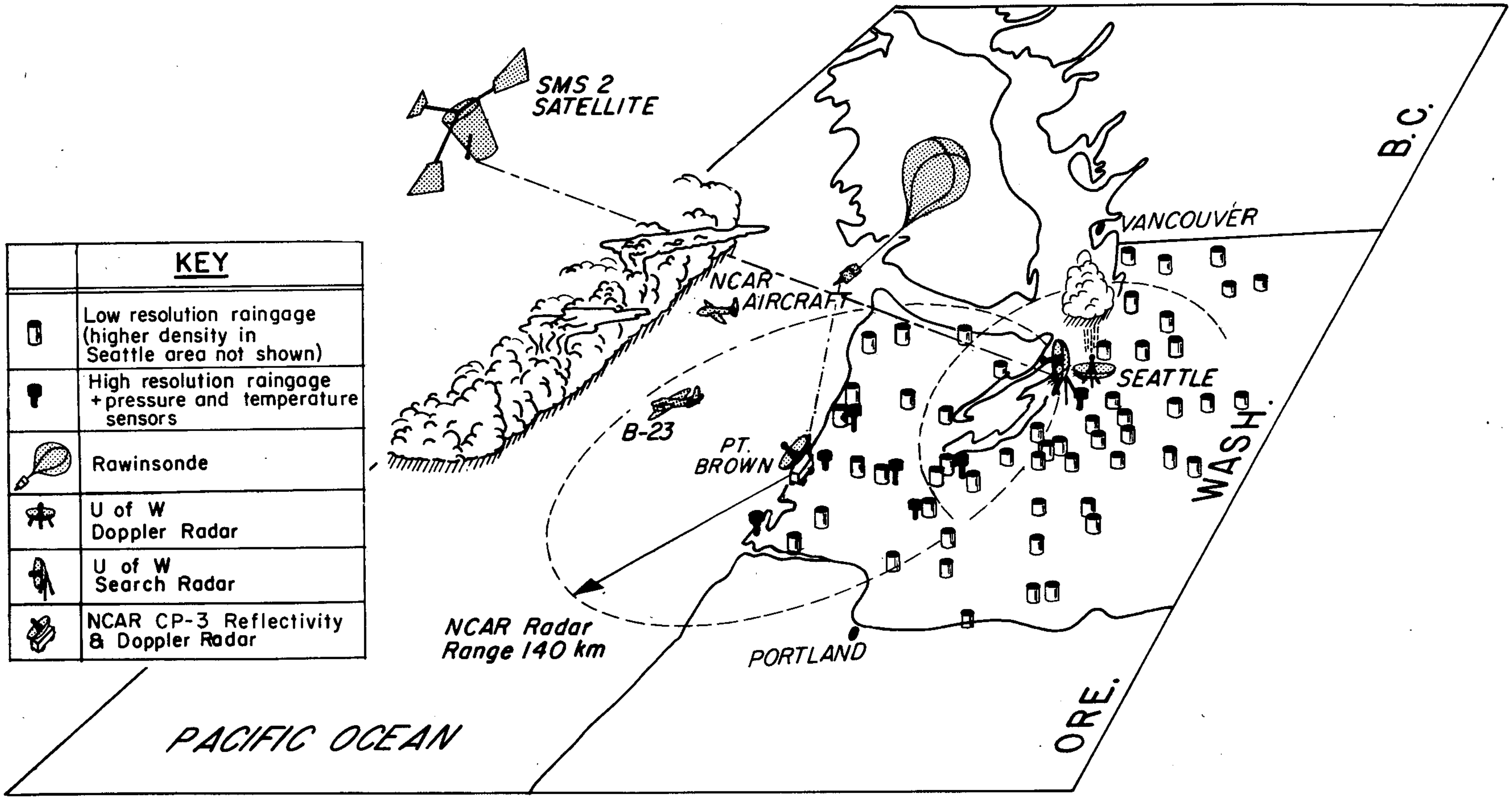

FIG. 1. Schematic of the observational facilities used in the CYCLES PROJECT.

TABLE 2. Characteristics of radars used in the CYCLES PROJECT.

	NCAR CP-3 radar	UW search radar	UW vertically pointing Doppler radar
Wavelength (cm)	5.45	3.2	3.2
Maximum power (kW)	372	250	7
Pulse repetition frequency (Hz)	1071	500	4000
Pulse length (μs)	1	1.75	0.25
Beam width (deg)	1.1	1	0.5
Range (km)	140	100	16 adjustable levels in vertical
Receiver bandwidth (MHz)	10	4	4
Antenna diameter (m)	3.7	2	3
Scan speed (rpm)	1–3	10–15	—
Presentation	PPI, RHI or time-height color display scans of reflectivity and Doppler velocities	PPI reflectivities	Spectra of fallspeeds of precipitation particles

heights above the radar. In this case the aircraft fly back and forth above the radar at various heights.

As a storm moves eastward and beyond the range of the CP-3 radar, it comes within range of UW search radar which is located in Seattle (Fig. 1). This radar can track the storms until they move into the Cascade Mountains. The rapid speed at which this radar is scanned (10–15 rpm) has proved useful in tracking small mescoscale features (Hobbs and Locatelli, 1978).

The UW vertically pointing Doppler radar, which is located in Seattle, provides measurements of the spectrum of fallspeeds of precipitation particles at 16 (adjustable) heights above the radar. On some occasions, the vertically pointing antenna for this radar is used to transmit the 250 kW of incoherent radiation from the UW search radar. This provides a time-height record of the radar echo pattern above the radar.

The principal aircraft used in the CYCLES PROJECT is the UW B-23. In the winters of 1974–75, 1975–76, 1976–77 and 1977–78, NCAR's Sabreliner aircraft was also used. The instruments which were aboard these two aircraft during the 1977–78 field project are listed in Table 3; the instrumentation used in other seasons was very similar. The B-23 and Sabreliner are particularly well instrumented for cloud microphysical and air motion measurements, respectively. Most of the measurements are displayed aboard the aircraft in real time, as well as being recorded on magnetic tape for subsequent analysis. A large number of the measurements made aboard the B-23 are telemetered to the UW Control Center where they are displayed in real time on strip charts. Both aircraft have two-way radio communication with the UW Project Director.

The two aircraft, which generally fly simultaneously, are directed by the Project Director into mesoscale features observed by the ground radars. The fast and high-flying capabilities of the Sabreliner make it particularly useful for obtaining an overview of the storms from high altitudes and for probing the higher clouds. The B-23, which is capable of flying in heavy icing conditions, is generally used to obtain measurements from just above ground level up to altitudes to ~5.5 km.

The large quantity of information available to the Project Director in real time allows him to direct the aircraft into the most interesting regions of the storms. This permits simultaneous airborne and radar measurements to be obtained for several hours in various mesoscale features associated with cyclonic storms as they move from over the Pacific Ocean, onshore and then over western Washington.

3. The mesoscale and microscale structure and organization of a cold front

We now turn to a description of a well-defined cold front that was documented using the facilities and techniques described above. Analysis of the measurements that were obtained has provided, for the first time, a detailed picture of the mesoscale and microscale processes associated with clouds and precipitation in cold fronts. The analysis begins with a brief description of the large-scale weather situation and the frontal structure as observed with serial rawinsondes. Radar data are then used to obtain a description of the large and small mesoscale organization of the precipitation. Air motions within mesoscale rainbands associated with the front are calculated from Doppler radar data, and the rates of condensation implied by these air motions are compared to the rainfall rates to obtain estimates of the precipitation efficiencies in the rainbands. The study concludes with a quantitative evaluation of the mechanisms for precipitation growth in the various regions of the system.

a. Synoptic setting

The cold front moved ESE through the CYCLES observational network on 17 November 1976; it was

TABLE 3. Measurements made aboard the two research aircraft used in the CYCLES PROJECT.

Measured parameter	Instrument	Range
(a) *The University of Washington's B-23*		
Total air temperature*	Rosemount platinum resistance	−70 to 30°C
Static air temperature*	In-house platinum resistance	−70 to 30°C
Dewpoint*	Cambridge thermoelectric type	−40 to 50°C
Pressure altitude*	Rosemount variable capacitance	150 to 1060 mb
True airspeed*	Rosemount variable capacitance	0 to 230 m s^{-1}
Aircraft heading	Sperry gyrocompass	0 to 360°
Ground speed and drift angle	Bendix Doppler navigator	0 to 600 kts; ±30°
Angle of attack	Rosemount potentiometer	±23°
Aircraft position and course plotter*	In-house (works off DME and VOR)	190 km
Time	Radio WWV and Systron Donner time code generator	
Altitude above ground	Radar altimeter	0 to 6 km
Horizontal winds	Computer product from true airspeed, heading, ground speed and drift angle	0 to 100 m s^{-1}
Weather radar	RCA (5 cm)	95 km
Air turbulence*	MRI differential pressure	0 to 10 $cm^{2/3}$ s^{-1}
Liquid water*	Johnson-Williams hot wire	0 to 2 g m^{-3} or 0 to 6 g m^{-3}
Precipitation particles	MRI metal foil	>250 μm
Precipitation particles	PMS precipitation probe	300 to 4500 μm
Cloud particles	PMS cloud probe	30 to 450 μm
Cloud particles*	PMS ASSP probe	3 to 60 μm
Cloud and precipitation particles	MRI Formvar replicator	—
Ice particle concentrations*	UW optical ice particle counter	0 to 1000 ℓ^{-1}
Ground communications	FM transceiver	190 km
Photography	Automax	1 s to 10 min
Vertical wind	Computer product of angle of attack, vertical aircraft speed and true airspeed referenced to vertical	−10 to 10 m s^{-1}
(b) *NCAR Sabreliner*		
Total air temperature	Rosemount platinum resistance	−70 to +30°C
Dewpoint	Cambridge thermoelectric	−30 to +50°C
Dewpoint	General eastern thermoelectric	−35 to +50°C
Pressure altitude	Rosemount variable capacitance	150 to 1060 mb
True airspeed	Rosemount variable capacitance	0 to 230 m s^{-1}
Magnetic heading	Sperry gyrocompass	0 to 360°
Aircraft velocity vector	Litton inertial navigation system	0 to 512 m s^{-1}
Aircraft position	Litton inertial navigation system	—
Horizontal air motions	Rosemount gust probe	0 to 512 m s^{-1}
Vertical air motions	Rosemount gust probe	−25 to 25 m s^{-1}
Cloud particles	PMS cloud probe	20 to 300 μm
Precipitation particles	PMS precipitation probe	200 to 3000 μm
Liquid water	Johnson-Williams hot wire	0 to 2 g m^3 or 0 to 6 g m^{-3}

* Data telemetered to CYCLES Control Center.

associated with a cyclone centered 1200 km to the north of Seattle (Fig. 2). The surface frontal passage at Pt. Brown on the Washington Coast occurred at 0730 PST. The wind shift accompanying the frontal passage at the surface appeared as a marked line of discontinuity in the PPI's of the Doppler velocity field at 0° elevation on the color display of the CP-3 radar. This line of discontinuity was used to determine the orientation of the surface front and to track its movement. During most of the study the front was oriented perpendicular to 114° azimuth from the radar and its component of motion in that direction was 13 m s^{-1}. During the latter part of the study, the orientation became more SW–NE and the speed slowed.

Fig. 3 shows a time-height section, derived from serial rawinsondes launched from Pt. Brown, of temperature, wind and relative humidity through the frontal system. The features depicted are typical of those associated with cold fronts. Temperatures were generally steady as the front approached but fell sharply behind the front. Low-level winds, within 70 km ahead of the cold front, were strong and southwesterly, with maximum velocities of over 25 m s^{-1} occurring at an altitude of 0.8 km. This low-level jet was similar to those described by Browning and Pardoe (1973), who found that the jets are important in supplying moisture to the frontal and prefrontal precipitation regions of cyclonic storms. Winds at and above the core of the jet had a component of motion perpendicular to the front equal to or greater than the speed of the front. In the boundary layer, below an altitude of 0.8 km, the wind speed decreased and the wind direction veered

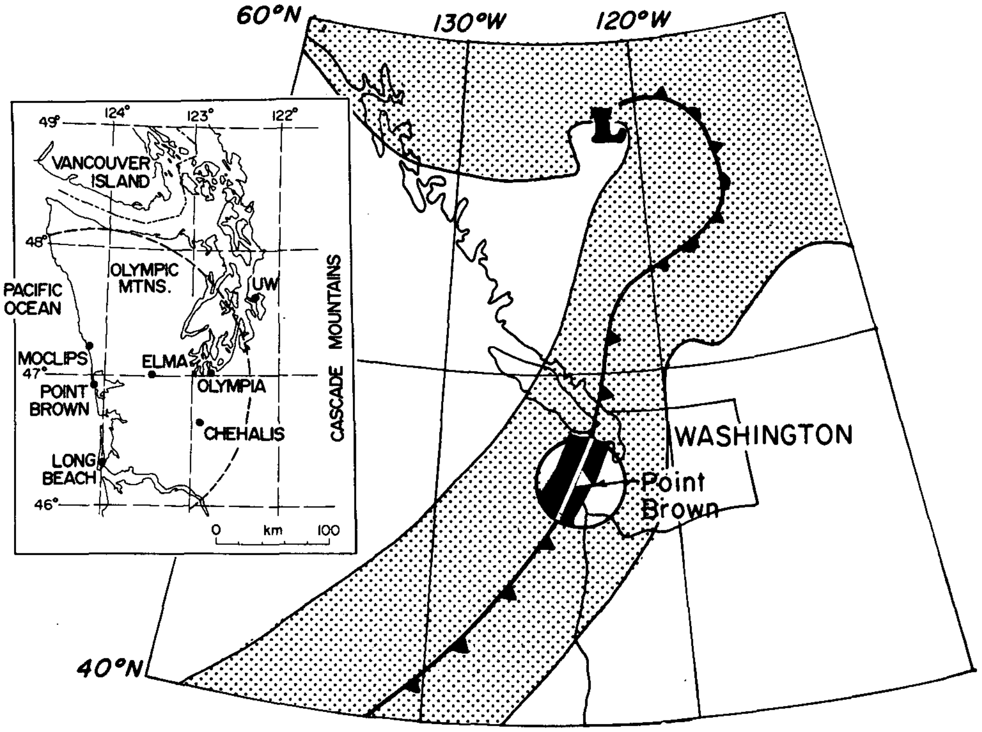

FIG. 2. The cloud shield (stippled area), the band of precipitation (black area) associated with the cloud front in the CYCLES observational area, and the surface position of the front at 0715 PST on 17 November 1976. The circle around Pt. Brown indicates the area of coverage of the CP-3 radar. The inset shows an expanded view of western Washington, the locations of the high-resolution precipitation gages (dots), and the range of the CP-3 radar over the land (dashed line).

with height so that the air flowed nearly parallel to the front and was overtaken by it. Behind the cold front, the winds backed with increasing height, indicating the advection of cold air. The relative humidity reached peak values in the vicinity of the cold front, while very dry regions were observed in the middle troposphere in the warm and cold air masses.

A time-height section of the wet-bulb potential temperature (θ_w) is shown in Fig. 4. The close packing of the isopleths behind the front indicates the rapid transition to cool, dry air. Regions where θ_w decreased with height, and therefore where the air was potentially unstable, are shaded in the diagram. A potentially unstable region was present in the lower levels both behind and immediately ahead of the front. In the warm airmass ahead of the zone of precipitation, there was potential instability in a layer in the lower-middle troposphere, a characteristic of a subtropical airmass.

Analyses of radar reflectivity and raingage data showed that several scales of organization of the precipitation could be distinguished. Several mesoscale bands of relatively high rainfall occurred embedded within an envelope of lighter rain. Rainfall was generally continuous throughout the entire period during which precipitation occurred; in this respect, this case differs from other CYCLES case studies previously reported, in which continuous rain between mesoscale rainbands was either absent or considerably lighter than in this case.

b. *Mesoscale organization of the precipitation*

The precipitation accompanying the passage of this frontal system consisted of a rainband ~50 km wide that was situated 50–80 km ahead of the cold front and a zone of precipitation up to 125 km wide that straddled the cold front and contained five mesoscale rainbands.

We will refer to the rainband well ahead of the cold front as the *warm-sector* band. Four of the rainbands in the zone of precipitation straddling the cold front were several tens of kilometers wide and will be referred to as *wide cold-frontal* rainbands. The other band, which was situated on and moved with the surface cold front, was only ~4 km wide; we will refer to this band as the *narrow cold-frontal* rainband.

A composite of the CP-3 radar reflectivity patterns associated with the warm-sector rainband and the four wide cold-frontal rainbands (labeled 1–4) are

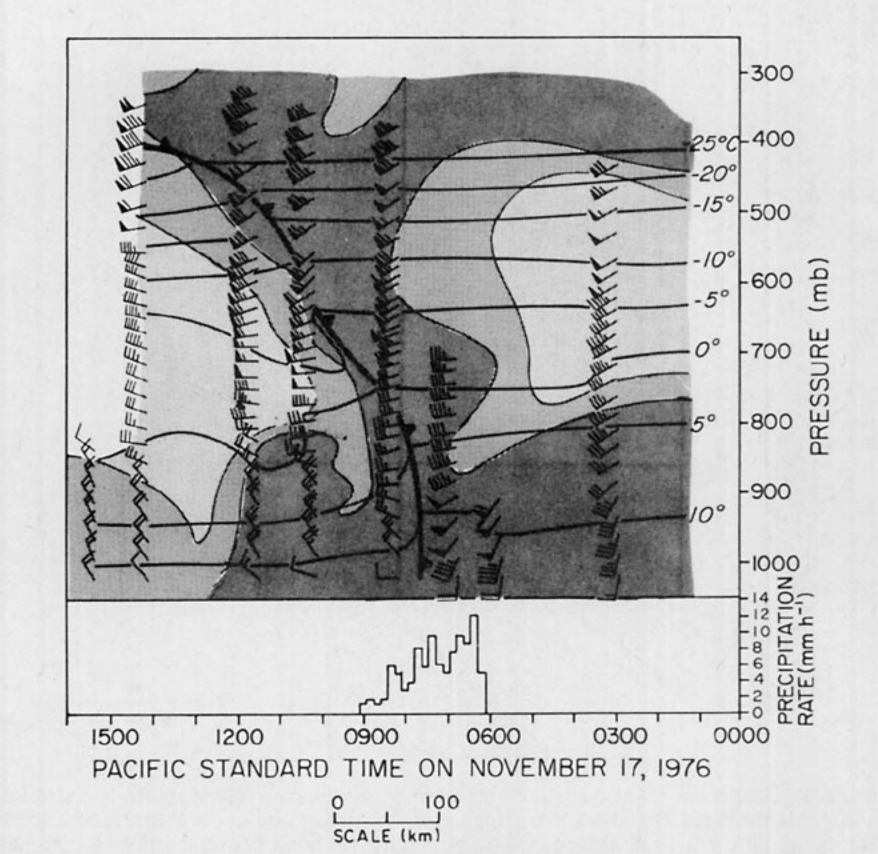

FIG. 3. Time-height cross section of temperature, wind and relative humidity derived from serial rawinsondes launched from Pt. Brown on 17 November 1976. The temperatures are shown by the contours and the winds by arrows (normal synoptic convention). The relation humidity (RH) is indicated by shading: lightest shading RH $< 30\%$, medium shading $30 \leq \text{RH} \leq 70\%$, darkest shading RH $> 70\%$. The precipitation rate at Pt. Brown is shown in the lower part of the figure.

shown in Fig. 5, and the effects of these rainbands on the precipitation at six of the high-resolution gages are indicated in Fig. 6.[3] It can be seen that each band could be discerned on the radar and produced a recognizable precipitation signature as it passed over the precipitation gages. Before moving inland, the warm-sector rainband consisted of two major sub-bands, as can be seen in Fig. 5b and in several of the precipitation rates shown in Fig. 6. We will subsequently refer to the sub-band near the leading edge of the warm-sector rainband as sub-band (a) and the sub-band behind it as (b).[4]

The radar reflectivity pattern produced by the narrow cold-frontal rainband is shown in Fig. 7, where it is labeled band 5. The effect of this rainband on precipitation is indicated in Fig. 6, where it can be seen that it produced a sharp increase in precipitation rate for a few minutes while it passed over Pt. Brown, Moclips, Elma, Chehalis and Olympia.

c. *Motions of the rainbands and their precipitation cores*

Previous studies (Browning and Harrold, 1969; Austin and Houze, 1972; Houze *et al.*, 1976a; Hobbs and Locatelli, 1978) have shown that rainbands in extratropical cyclones contain within them numerous smaller mesoscale and cumulus-scale cores of precipitation (tens–hundreds of square kilometers); following Hobbs and Locatelli, we will call these *precipitation cores*.

The warm-sector rainband, the wide cold-frontal rainbands and the narrow cold-frontal rainband in the frontal system of 17 November 1976, contained precipitation cores which covered horizontal areas from 25 to 300 km^2. These cores were tracked with the radar for up to 50 min. The precipitation cores in the warm-sector and wide cold-frontal rainbands were irregular in shape and randomly positioned in space. By contrast, the precipitation cores in the

---

[3] The rainbands were generally superimposed on relatively high levels of large-scale "background" precipitation. The rainbands were identified and tracked from the radar data rather than the raingages.

[4] Each of the sub-bands could be considered as a separate warm-sector rainband.

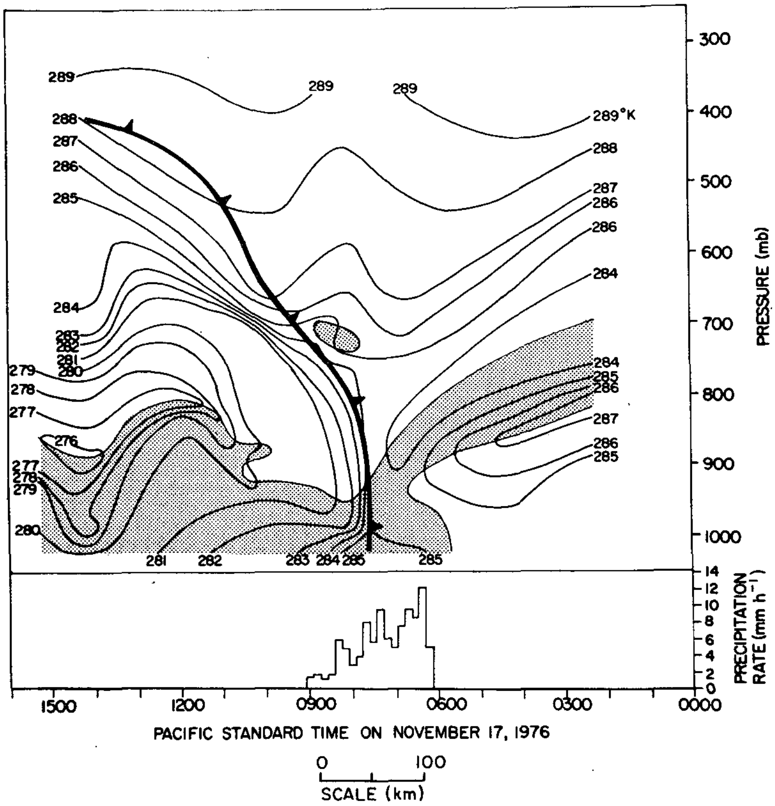

FIG. 4. As in Fig. 3 except for wet-bulb potential temperature (θ_w). The shaded area indicates the region of potential instability ($\partial\theta_w/\partial z < 0$).

narrow cold-frontal rainband (rainband 5) had ellipsoidal shapes with similar orientations (Fig. 8); the other narrow cold-frontal bands which we have studied have shown similarly organized small mesoscale structures (Hobbs and Biswas, 1979).

Some characteristics of the precipitation cores within the wide and narrow cold-frontal rainbands and the warm-sector rainband are listed in Table 4. Inspection of the data in Table 4 reveals that the precipitation cores in the warm-sector band and the four wide cold-frontal bands moved, on average, toward 64° at a speed of 29 m s^{-1}.

The total vector velocities and the velocities normal to the cold front of the envelope of precipitation associated with the front, with the wide and narrow cold-frontal and warm-sector rainbands, with the precipitation cores and with the upper level cloud shield (determined from satellite images) are shown in Fig. 9. We estimated that the accuracy of these velocities is $\sim\pm2.5$ m s^{-1}. The normal velocities of the surface frontal position, the envelope of the frontal precipitation, the narrow cold-frontal rainband and its precipitation cores and the upper level cloud shield, were essentially the same. However, the normal velocities of the wide cold-frontal and warm-sector rainbands and their precipitation cores were significantly greater than the other features. Careful viewing of the radar data covering time periods of up to 10 h revealed clearly that the wide cold-frontal and warm-sector rainbands advanced relative to the other features; this can be seen in part from the radar data shown in Fig. 10.

The color displays of reflectivity and Doppler velocities, provided by the CP-3 radar, clearly showed that the motions of the wide cold-frontal and warm-sector rainbands were greater than that of the wind shift line which marked the position at the surface of the cold front itself. One of the wide cold-frontal rainbands (rainband 1), in fact, advanced from a position behind the surface cold front and the narrow cold-frontal rainband to a position immediately ahead of them during the period of our observations. The warm-sector rainband displayed a different evolution and motion: sub-band (b) formed near the surface cold front and sub-band (a) developed ahead of sub-band (b). Both sub-bands advanced relative to the front. A third, incipient sub-band subsequently formed and intensified ahead of sub-band (a).

The maximum heights of the precipitation cores in the rainbands were determined from three-dimensional radar observations. The results are shown in Table 5, where it can be seen that the tops of the precipitation cores in the warm-sector band and the wide

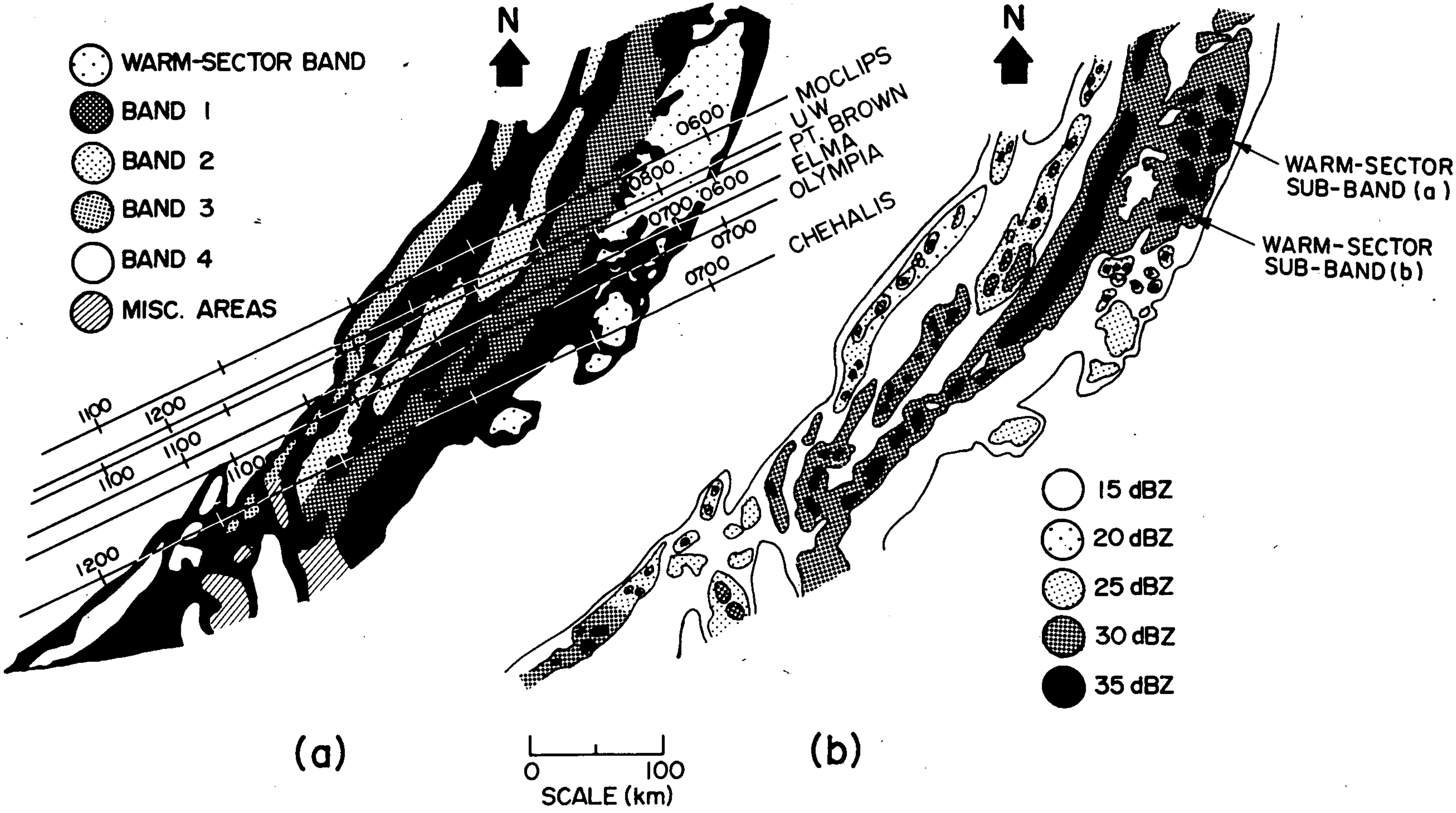

FIG. 5. (a) Composite horizontal radar reflectivity pattern showing the warm-sector rainband and the wide cold-frontal rainbands (labeled 1–4) over western Washington on 17 November 1976. The paths of the system over the six high-resolution precipitation gages (whose locations are shown in Fig. 1) are indicated by the six straight lines. Shown on each line are the times that various portions of the system were over the given gage. The precipitation rates at each of the gages are shown in Fig. 6. (b) Reflectivity intensities of the rainbands shown in (a).

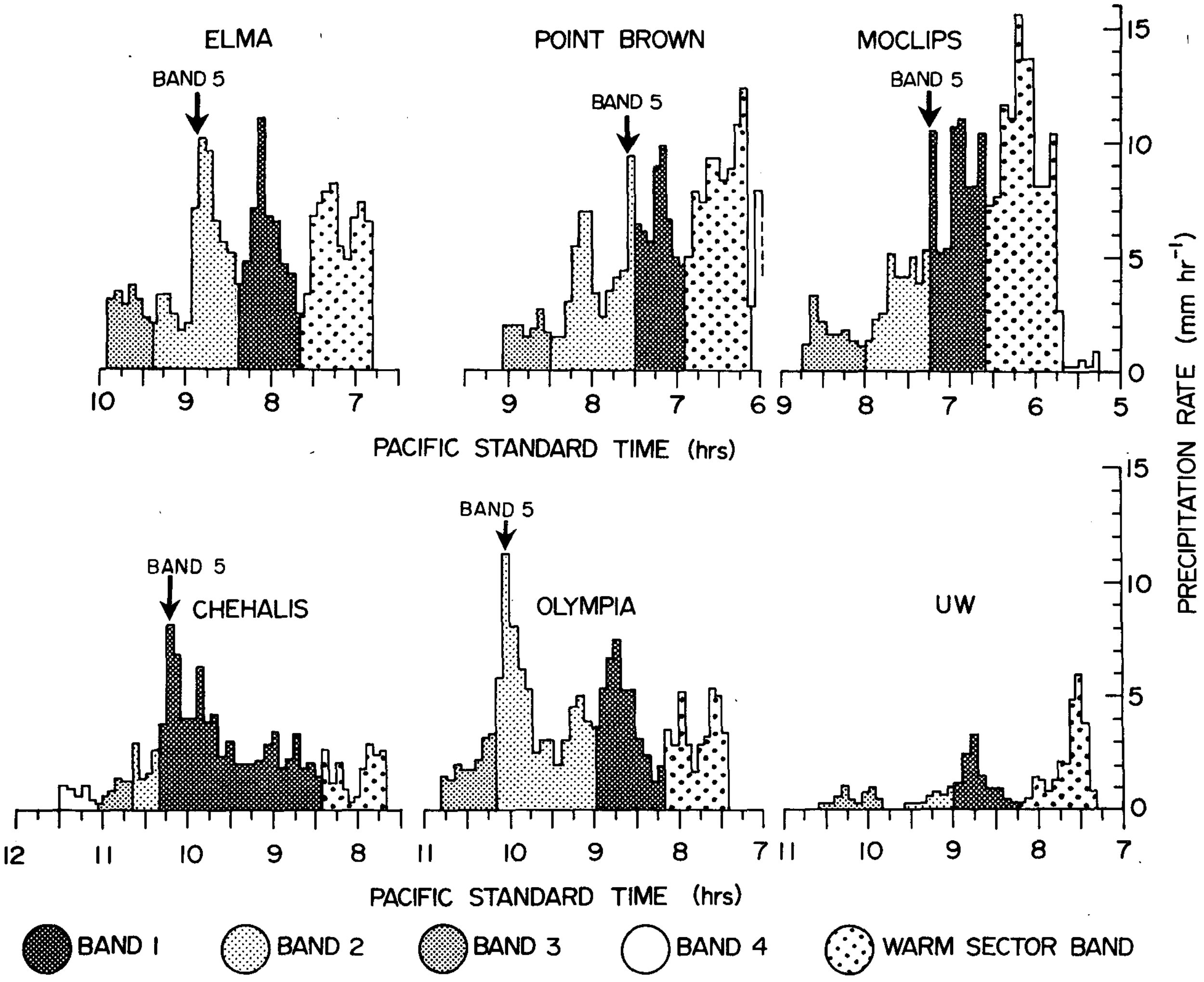

FIG. 6. Precipitation rates at six of the high-resolution gages shown in Fig. 2. The portion of the precipitation due to the warm-sector and wide cold-frontal (1–4) rainbands are indicated by the same shading as in Fig. 5a. The arrow shows the time that the narrow cold-frontal rainband (5) passed over each gage.

cold-frontal bands were between ~5 and 6 km, while the narrow cold-frontal band had tops between 1.5 and 4.5 km.

The relationships between the horizontal winds and the motions of the rainbands and their precipitation cores can provide an indication of the levels at which the precipitation particles in a rainband originate. Using the technique described by Locatelli and Hobbs (1978), the Doppler radar measurements were used to deduce the wind directions through the frontal system (Fig. 11). Also shown in Fig. 11 are the wind directions and speeds from four rawinsondes launched from Pt. Brown during the passage of the system, the boundary of the precipitation particles detected by the radar, the locations of the rainbands deduced from the radar reflectivity data, and the location of the cold front at 1715 PST (15 min before the surface front passed through Pt. Brown).

It can be seen from Fig. 11 that there was cold advection behind the front, as indicated by the backing of the winds with height, and that the main wind shifts occurred in the lowest kilometer, with the largest wind shift at the surface. At the leading edge of the system there was a cloud and precipitation "overhang" ~1 km thick which extended about 30 km ahead of the main body of the system. This overhang was probably due to "blow-off" from the warm-sector band. There was also an overhang, about 5 km thick, which extended some 90 km behind the main body of the frontal system, from which precipitation fell but evaporated before reaching the surface.

The velocities of the wide cold-frontal rainbands and their precipitation cores [~29 m s^{-1}, or 56 kt, toward 65° (see Fig. 9)] were similar to the velocities of the winds between ~3 and 6 km in altitude (Fig. 11). Hence, these rainbands were steered by the

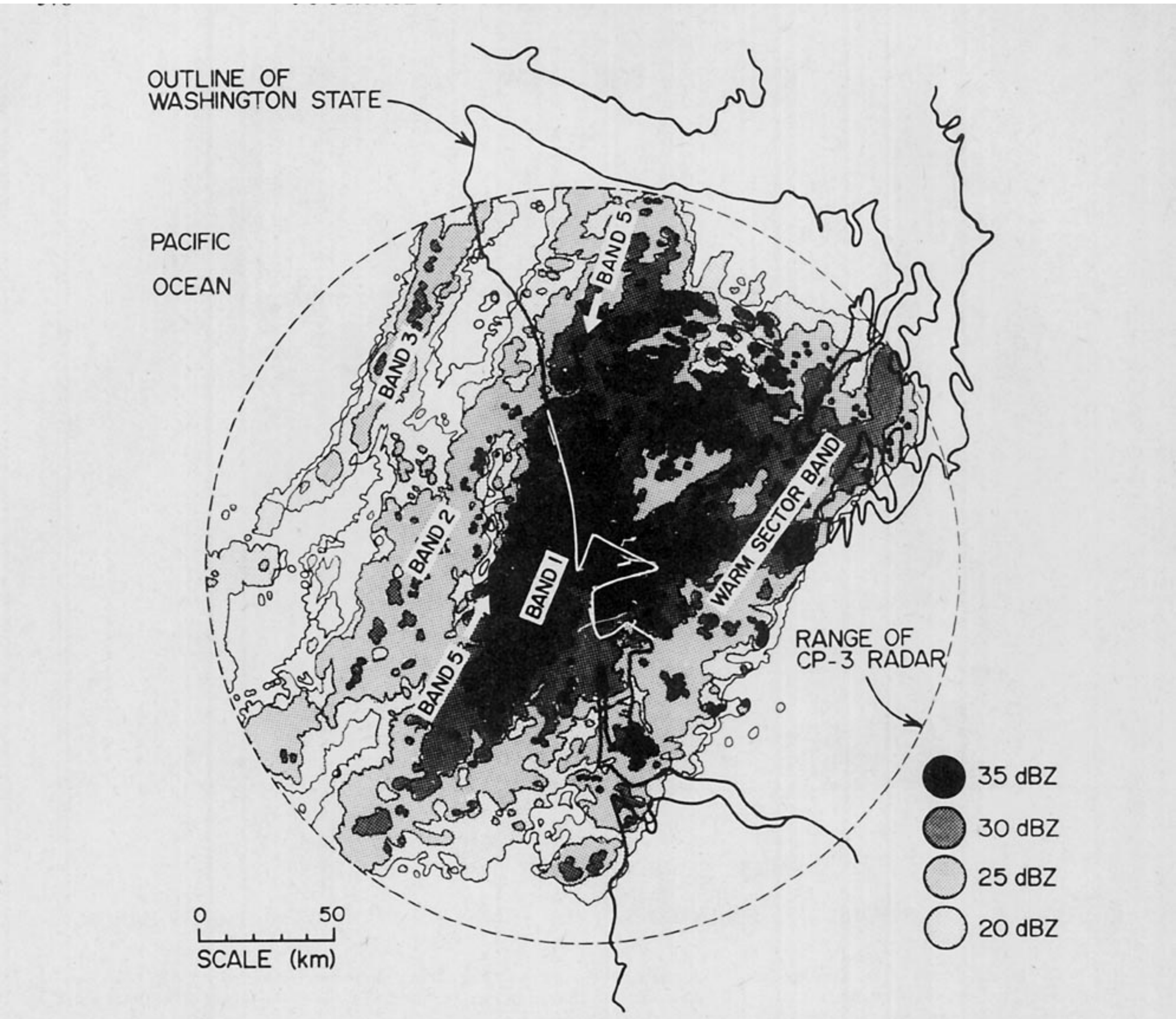

FIG. 7. The horizontal radar reflectivity pattern at 0700 PST 17 November.

winds between 3 and 6 km, that is, near their upper levels. The velocity of the precipitation cores in the warm-sector rainband was $\sim$28 m s^{-1} toward 66°. This velocity is similar to the winds at both the lower and upper levels of the band. We will see later that there is additional evidence that the warm-sector band was steered by winds in both the upper and lower levels.

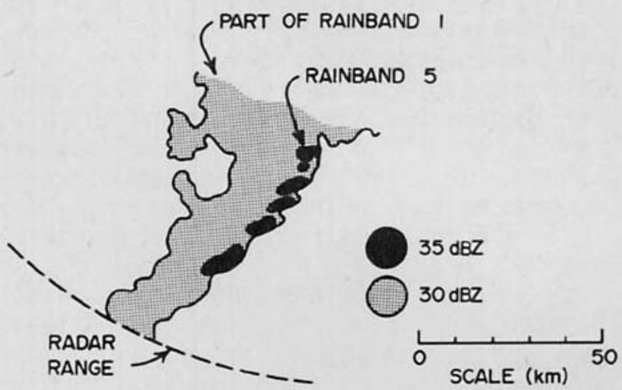

FIG. 8. Part of the horizontal radar reflectivity pattern at 0822 PST showing the organization of the strongest precipitation cores (black areas) in the narrow cold-frontal rainband (5).

The velocity of the precipitation cores in the narrow cold-frontal rainband was $\sim$18 m s^{-1} (or 35 kt) toward 85° (see Fig. 9). The only location where the winds have this velocity is within the narrow cold-frontal rainband itself (see Fig. 11). Hence, unlike the wide cold-frontal bands, the narrow cold-frontal rainband was not steered by upper level winds.

d. Air motions associated with the rainbands

Doppler velocity data measured with the CP-3 radar as the radar beam was oriented perpendicular to each rainband were used to obtain the cross-band component of the horizontal winds in vertical

TABLE 4. Characteristics of the precipitation cores within the wide cold-frontal (1–4) and narrow cold-frontal (5) rainbands and the warm-sector rainband.

Rainband number	Precipitation core number	Area of precipitation core (km^2)	Speed of precipitation core (m s^{-1})	Direction of motion of precipitation core (deg)	Time tracked (min)
1	1	300	37	46	14
	2	64	32	64	16
	3	300	25	70	37
Averages		200	31	60	
2	1	100	29	55	29
	2	60	18	60	20
	3	150	28	62	30
	4	150	29	66	50
	5	60	20	80	16
	6	150	27	70	15
	7	200	36	62	22
	8	60	30	65	45
Averages		116	27	65	
3	1	40	37	64	28
	2	60	33	63	28
	3	40	27	66	15
	4	20	43	62	14
	5	80	42	64	15
	6	80	35	63	15
	7	220	35	55	15
	8	300	24	65	16
	9	80	34	60	38
	10	200	27	70	16
	11	50	34	64	38
	12	200	38	68	14
	13	100	39	65	15
Averages		113	34	64	
4	1	30	34	65	29
	2	30	30	62	15
	3	150	37	64	30
	4	25	27	64	15
Averages		59	32	64	
5	1	25	22	90	14
	2	45	15	90	30
	3	100	12	90	112
	4	40	12	95	21
	5	25	14	90	22
	6	25	15	90	22
	7	200	15	85	29
	8	150	23	85	12
	9	10	20	80	15
	10	40	21	84	15
	11	40	19	80	31
	12	30	21	80	31
	13	16	18	85	31
	14	60	20	76	31
	15	64	20	82	15
Averages		58	18	85	
Warm-sector	1	100	32	60	14
	2	25	18	60	15
	3	100	32	65	23
	4	250	28	60	16
	5	250	32	66	42
	6	200	30	68	76
	7	150	32	65	22
	8	20	26	80	17
	9	20	25	75	17
	10	70	33	64	16
	11	25	28	66	16
	12	225	28	65	76
	13	25	27	70	30
	14	40	27	65	16
	15	100	29	67	15
Averages		106	28	66	

planes perpendicular to the rainbands. Vertical velocities of the air were calculated by assuming that only minor divergence occurred in the component of the wind parallel to the rainbands and by applying the equation of mass continuity to the divergent cross-band component. The values of the cross-band wind component were plotted in the vertical cross-section planes, and subjective isotach analyses were performed. This step tended to smooth out any cumulus-scale irregularities in the wind field. Some further smoothing occurred when values of the speed of the cross-band wind component were then obtained from the isotach analyses at rectangular grid points, and horizontal convergences were computed over horizontal grid spacings of 2.6, 5.2 and 10.4 km. These divergences were integrated upward in ⅓ km steps from the surface, where a vertical velocity of zero was assumed. The resulting vertical velocities were combined with the cross-band component of the horizontal wind to produce vectors representing the instantaneous airflows in vertical planes oriented perpendicular to the rainbands. The airflows that are shown with the convergence-divergence fields in Figs. 12–14 were derived using a horizontal grid spacing of 5.2 km. Airflows produced using the grid spacings of 2.6 and 10.4 km were very similar, but seemed noisy and overly smoothed, respectively. Because of the smoothing of the cumulus-scale irregularities, the resulting divergences and airflows are those associated primarily with the mesoscale, band-shaped organization.

The various assumptions that were made to obtain the vertical motions lead to increasing errors in the vertical air velocities toward higher altitudes. No attempt was made to correct or truncate these errors. Therefore, above an altitude of ~4 km, the vertical motions shown in the figures should be interpreted with caution and probably only in a qualitative way. The assumption of nondivergence

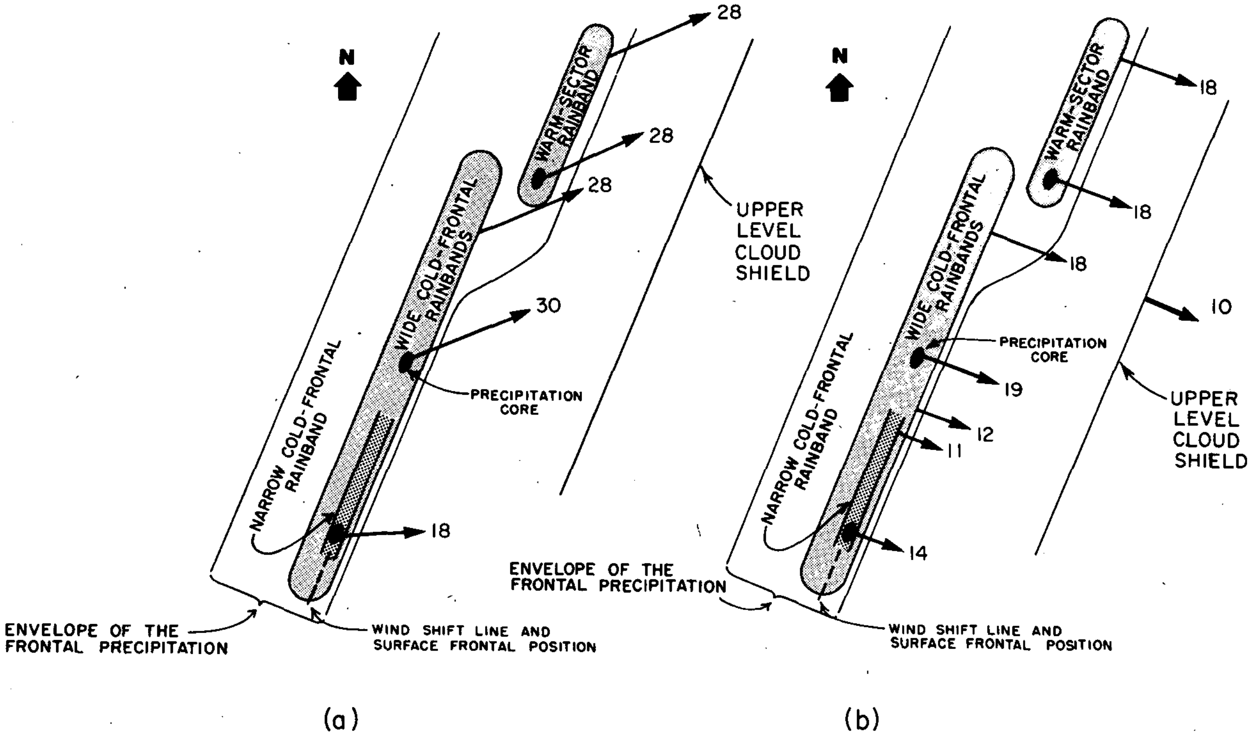

FIG. 9. (a) Velocity vectors (m s^{-1}) of the cloud shield, the envelope of the frontal precipitation, the wide and narrow cold-frontal rainbands, and the warm-sector rainband and the precipitation cores (heaviest shaded areas). (b) Velocities normal to the cold front. Diagram is not drawn to scale and does not show relative positions of the various features.

in the direction parallel to the rainbands was checked when the rainbands over the radar by comparing the component of the velocity (measured with the CP-3 radar) to the NNE with that to the SSW. The wind in this direction was generally slightly convergent, but the magnitudes of divergence were almost always less than 1.7×10^{-4} s^{-1}, and usually less than 1.0×10^{-4} s^{-1}. These values are much less than the divergence of the cross-band wind field associated with the rainbands, which generally ranged from 3×10^{-4} to 19×10^{-4} s^{-1}. In addition, direct measurements of divergence from 0 to 3 km altitude in the regions containing the rainbands were obtained from the CP-3 radar data using the VAD technique discussed by Herzegh and Hobbs (1980). These measurements showed that the convergence (divergence) in the component of the wind parallel to the rainbands was generally less than 20% of the magnitude of the convergence (divergence) in the cross-band wind component. These results indicate that the rainbands were roughly two-dimensional and that the general airflow pattern in the rainbands can be obtained through measurements of the cross-band wind velocity component.

Fig. 12 shows the derived airflow and the convergence-divergence field associated with the warm-sector rainbands. The warm-sector sub-band (a) appeared on the radar as a strong, organized line of echoes; by contrast, the echoes associated with the warm-sector sub-band (b) were arranged in a broader banded region and were not organized in a well-defined line. Strong horizontal convergence, with values nearly reaching 10^{-3} s^{-1} were associated with sub-band (a) and occurred from the ground up to 2.5 km altitude. Above this layer, a deep layer of divergence occurred. The airflow pattern relative to the motion of sub-band (a) shows that air flowed into the warm-sector rainband at low levels from ahead of the rainband. This air rose sharply above sub-band (a) to ~4 km altitude. Maximum calculated upward velocities in this region were ~2 m s^{-1}. Above 4 km, upward velocities decreased markedly, and the lifted air flowed toward the rear of the rainband, trailing behind the surface line of rain. The airflow pattern associated with sub-band (a) is remarkably similar to (although much less vigorous than) the inflow-updraft-anvil structure of squall lines, such as that described by Houze (1977).

The divergence pattern associated with sub-band (b) (Fig. 12) was similar to that of sub-band (a), although the layers of convergence and divergence were less clearly differentiated. The airflow in sub-band (b) was also similar to that associated with sub-band (a), although the updrafts were weaker and multiple. These results agree with the less organized appearance of sub-band (b) seen with radar.

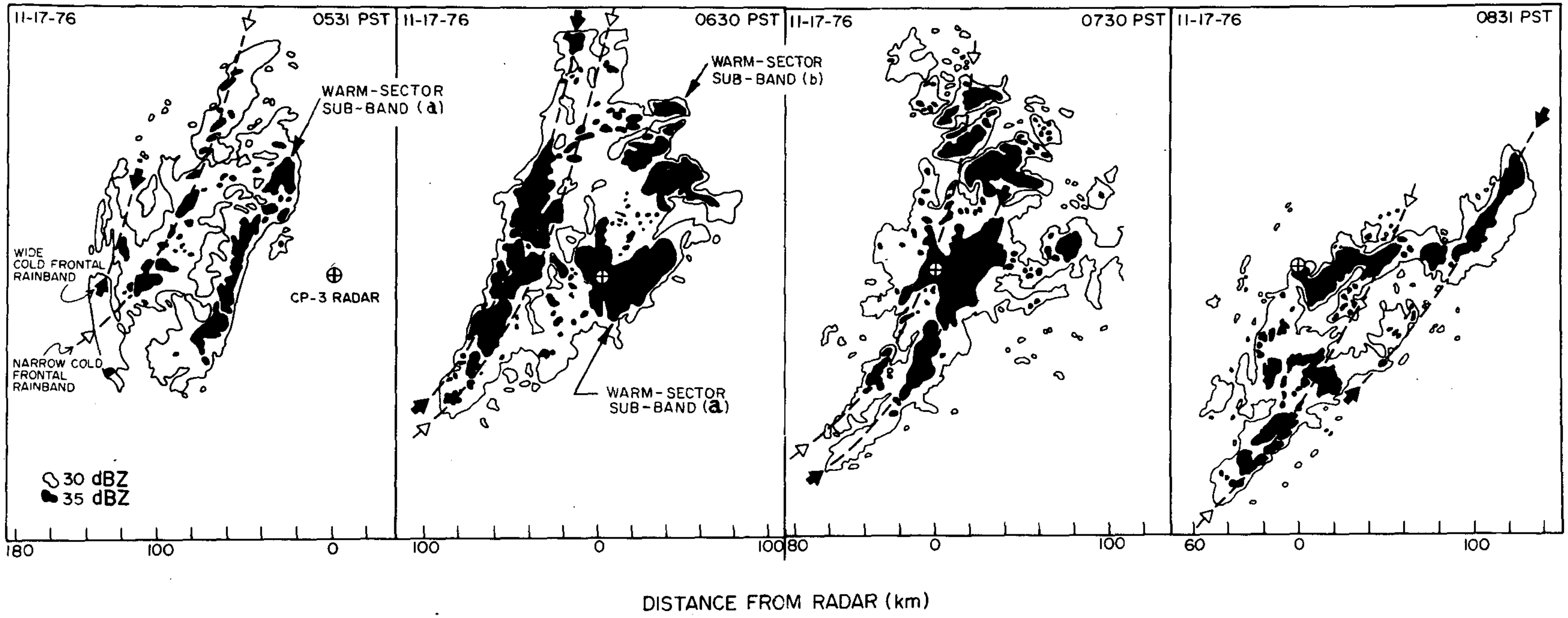

FIG. 10. Motions of the wide cold-frontal rainband (1) and the narrow cold-frontal rainband as revealed by the CP-3 radar. It can be seen that the wide cold-frontal rainband moved faster than the narrow cold-frontal rainband, so that it caught up with and eventually overtook the narrow cold-frontal band. Warm-sector sub-bands (a) and (b), partially obscured by ground clutter near the radar, are also visible.

TABLE 5. Maximum heights of the precipitation cores in the rainbands associated with the cold front.

Type of rainband	Rainband number	Maximum height of precipitation cores (km)
Warm-sector	—	6.1
Wide cold-frontal	1	6.1
	2	5
	3	5
	4	—
Narrow cold-frontal	5	1.5–4.5*

* Maximum height was somewhere between the two radar scan heights listed.

A region of strong low-level convergence and a vigorous updraft occurred immediately ahead of the warm-sector sub-band (a) (Fig. 12), but it produced relatively little precipitation at the ground. This feature was associated with the development of new convective towers in a new warm-sector sub-band ahead of the older sub-bands, similar to the behavior of convection in squall line systems. Interestingly, the airflow associated with this feature showed no middle-level, rearward flow corresponding to the outflow in the anvil of mature convection in a squall line.

No organized downdraft appears in the airflow pattern in Fig. 12; a region of divergence, however, did occur in the boundary layer in sub-band (b). That regions of more marked divergence existed near the surface could be seen from the Doppler radar data; however, they were not intersected by the plane perpendicular to the rainbands. Matejka *et al.* (1980) found evidence of downdrafts in warm-sector rainbands that were somewhat more strongly developed than that described here.

Fig. 13 shows the divergence field and the airflow associated with the wide cold-frontal rainband 1 at 0630 PST. At this time, most of this rainband was situated ahead of the cold front. The convergence field differed markedly from that associated with the warm-sector rainband. Except for a shallow layer of convergence at the ground, the lower layer, up to 3 km altitude, wsa characterized by weak divergence. However, a layer of moderately strong convergence (with maximum magnitudes around 5×10^{-4} s^{-1}) between 3 and 5 km altitude produced considerable ascent aloft with maximum velocities calculated to be ~1 m s^{-1}. The airflow through the rainband was generally from the front toward the rear; the rainband at the ground is correspondingly displaced to the rear of the zone of ascent above 4 km altitude.

Fig. 14 shows the divergence field and the airflow associated with the narrow cold-frontal rainband 5 and the two wide cold-frontal rainbands that followed it (rainbands 2 and 3). The narrow cold-frontal rainband was associated with a strong updraft, ~5 km in width and, at 1.5 km altitude, 1.2 m s^{-1} in magnitude, which originated in a region of strong convergence (up to 1.9×10^{-3} s^{-1}) within the lowest kilometer of the atmosphere at the surface cold front. Air ahead of the cold front flowed from the SSW in a low-level, moist jet almost parallel to the front (Fig. 11); relative to the front, the air in this jet in the lowest 500 m moved toward the front into the surface pressure trough where it ascended in a narrow updraft. At 3 km altitude, the updraft encountered much stronger winds from the west (Fig. 11) and was carried off to the east relative to the front (Fig. 14). (The upward air velocities at altitudes > 3 or 4 km above the narrow cold-frontal rainband in Fig. 14 are probably unreliable, due to errors

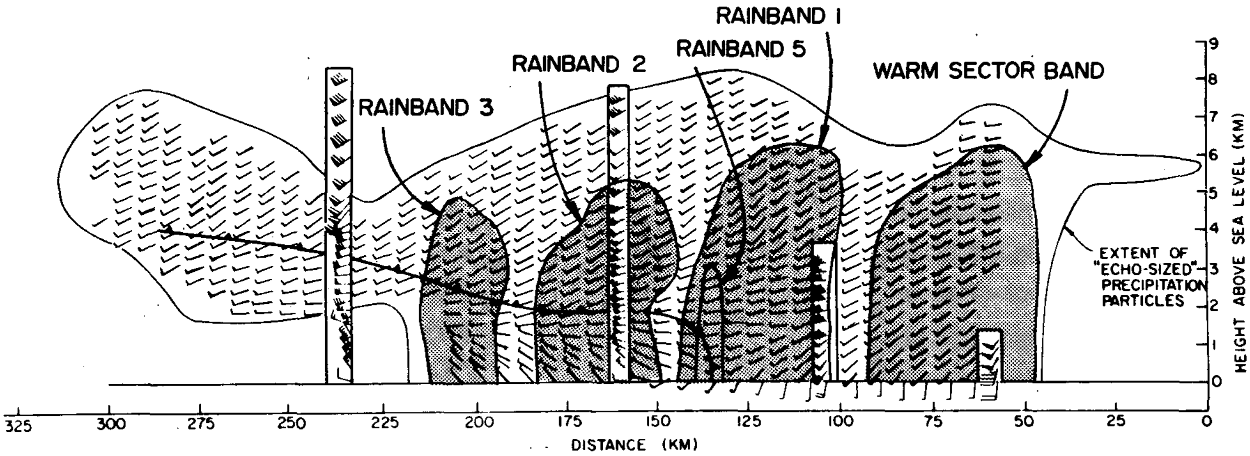

FIG. 11. Cross section perpendicular to the surface cold front of the frontal system through Pt. Brown on 17 November 1976. The detailed horizontal wind field (shown by the small arrows which indicate wind directions only) are derived from Doppler radar measurements. Serial rawinsonde measurements (showing wind directions and speeds in knots using conventional symbols) are plotted within the rectangular boxes. The warm-sector rainband, the wide cold-frontal rainbands (1–3), the narrow cold-frontal rainband (5) and the position of the front (at 0715 PST) are also shown.

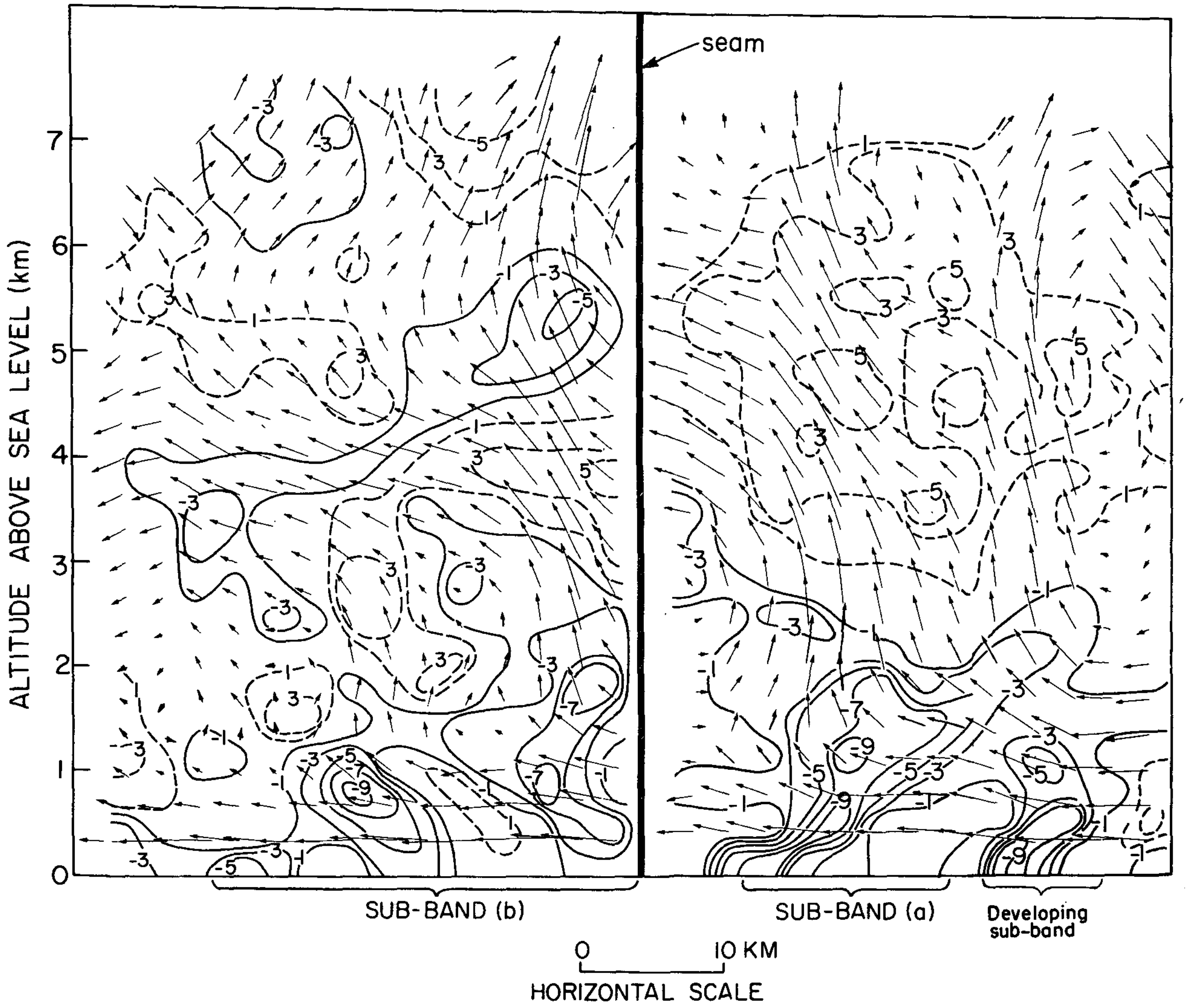

FIG. 12. Cross section through the width of the warm-sector rainband. The arrows show the calculated streamflow relative to the motion of the band (the lengths of the arrows represent 5 min displacements). The continuous lines show the calculated convergence and the dashed lines the calculated divergence (10^{-4} s^{-1}). To the right of the seam the computations are for 0530 PST, to the left for 0600 PST. The motion of the rainband was toward the right.

accumulated in the vertical integration.) A downdraft, ~5 km in width and 0.5 m s^{-1} in magnitude, was present between 1.5 and 3 km in altitude immediately ahead of the updraft region. At the base of the downdraft, values of divergence reached 1.1×10^{-3} s^{-1}. The coupling of convective updrafts and downdrafts in narrow cold-frontal rainbands is likely an integral mechanism in the formation of the characteristic, small-mesoscale organization of precipitation in narrow cold-frontal bands reported by Hobbs and Biswas (1979) and shown in Fig. 8.

Fig. 14 shows that air within the cold airmass had little motion relative to the cold front, but that air above the cold front flowed back, relative to the front, and ascended. This ascent, generated largely by convergence along the upper level cold front, occurred at altitudes from 2 to 5 km and was concentrated in two regions that corresponded roughly to the positions of the wide cold-frontal rainbands 2 and 3 at the surface. The winds at these levels are similar to the motion of the precipitation cores in rainbands 2 and 3, and it will be shown in Section 3f that precipitation particles in the wind cold-frontal rainbands were forming in these regions of ascent aloft.

The Sabreliner aircraft traversed the frontal region at altitudes of 4.5, 5.5 and 6.4 km, and the vertical air motions measured aboard the aircraft confirm several aspects of the airflow patterns shown in Figs. 12–14. For example, although the measured updraft speeds fluctuated rapidly at 4.5 km altitude (Fig. 15a), the trends of the measurements indicate that the rainbands contained broad regions of upward motion at this altitude. The updrafts in the warm-sector

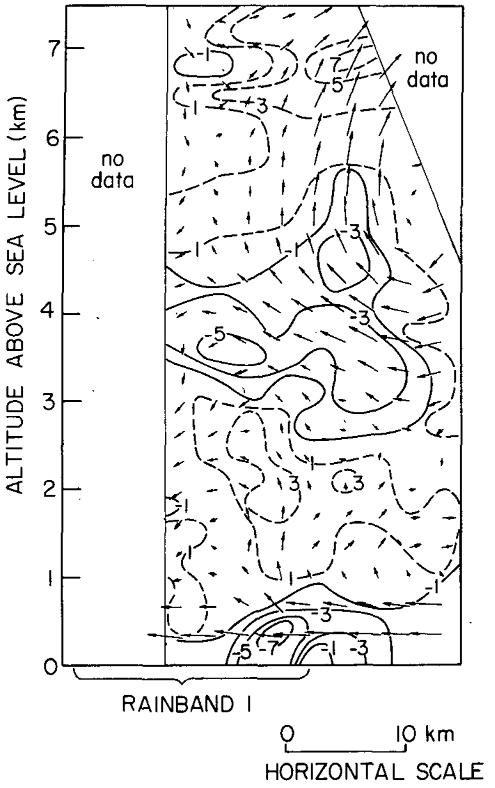

FIG. 13. Cross section through the wide cold-frontal rainband 1 showing the streamflow *relative to the motion of this rainband* at 0630 PST. The arrows represent 5 min displacements. The continuous lines show the calculated cross-band convergence and the dashed lines the calculated divergence (10^{-4} s^{-1}). The motion of the rainband was toward the right.

band reached ~90 cm s^{-1} in the front portion of the band, and in the cold-frontal rainband 1 they reached ~60 cm s^{-1}.[5]

Patterns of vertical velocities similar to those measured at 4.5 km were measured at 5.5 km. However, the measurements obtained from the aircraft at 6.4 km (Fig. 16a) suggest that the vertical motions associated with the warm-sector band were weak at this altitude. Several separate regions of upward and downward motions were observed; these motions may have been associated with upper level generating cells. At 6.4 km the motions in the wide cold-frontal rainbands 1 and 2 were still generally upward.

e. Condensation rates and precipitation efficiencies of the mesoscale rainbands

The calculations of the fields of vertical motion (described above) enable comparisons to be made between the rates of condensation of vapor in the rainbands and the precipitation rates. Such comparisons can then be used to estimate the efficiencies with which precipitation is produced in the rainbands.

Precipitation rates were calculated in two ways. A measure of the total precipitation rate in a rainband was obtained directly from precipitation gage data as the rainband passed over Pt. Brown. An instantaneous measure of the total precipitation rate in a strip of unit width oriented perpendicular to a rainband was also obtained from radar reflectivities at 0° elevation angle in the same cross section as that used for calculating the vertical motions. The reflectivities were converted to rainfall rates using relations developed through comparisons of the CP-3 radar reflectivities with ground-based disdrometer and raingage data in several extratropical cyclones during the project. Comparison of precipitation rates at Moclips deduced from radar reflectivities in the case discussed here with rainfall rates measured by the Moclips tipping gage showed good agreement: the largest discrepencies noted were approximately ±25% with no consistent bias toward higher or lower values.

Rates of condensation were calculated by performing a volume integral of the local condensation rate over those regions of the cross section where ascending motions that produced clouds were associated with the mesoscale rainband. A moist-adiabatic lapse rate was assumed through the regions of ascent. In addition, since the moisture that was being condensed by the air motions at the time the velocity data were obtained did not precipitate instantaneously, it was necessary to assume, for the purpose of calculating the precipitation efficiences, that the airflow and the precipitation rate associated with the rainband were in steady state. The two values of the precipitation rate used for each rainband in the calculation of the precipitation efficiency (one simultaneous with the velocity data used to deduce the air motions over the Pacific Ocean and the other that occurred as the rainbands reached the coast ~1 h later) lead to similar efficiences. This indicates that the steady-state assumption was valid offshore at least over a time period of ~1 h.

Some latitude exists in defining the edges of the rainbands, and this subjectivity introduced some additional uncertainties into the calculations of precipitation efficiencies. By using both radar and raingage data, a range of values for the total precipitation rates associated with each rainband was obtained. The boundaries of the volumes in which condensation was occurring due to ascent were similarly difficult to define precisely. The lower boundary of a volume was taken to be cloud base. Although vertical velocities determined by the convergence method become less reliable with increasing altitude, the decreasing amounts of water vapor in saturated air at higher altitudes cause the

---

[5] The accuracy of these measurements, from which the long-term mean vertical velocity has been removed, is mainly dependent upon the high-speed response of the gust probe system aboard the Sabreliner and is ±30 cm s^{-1} or better.

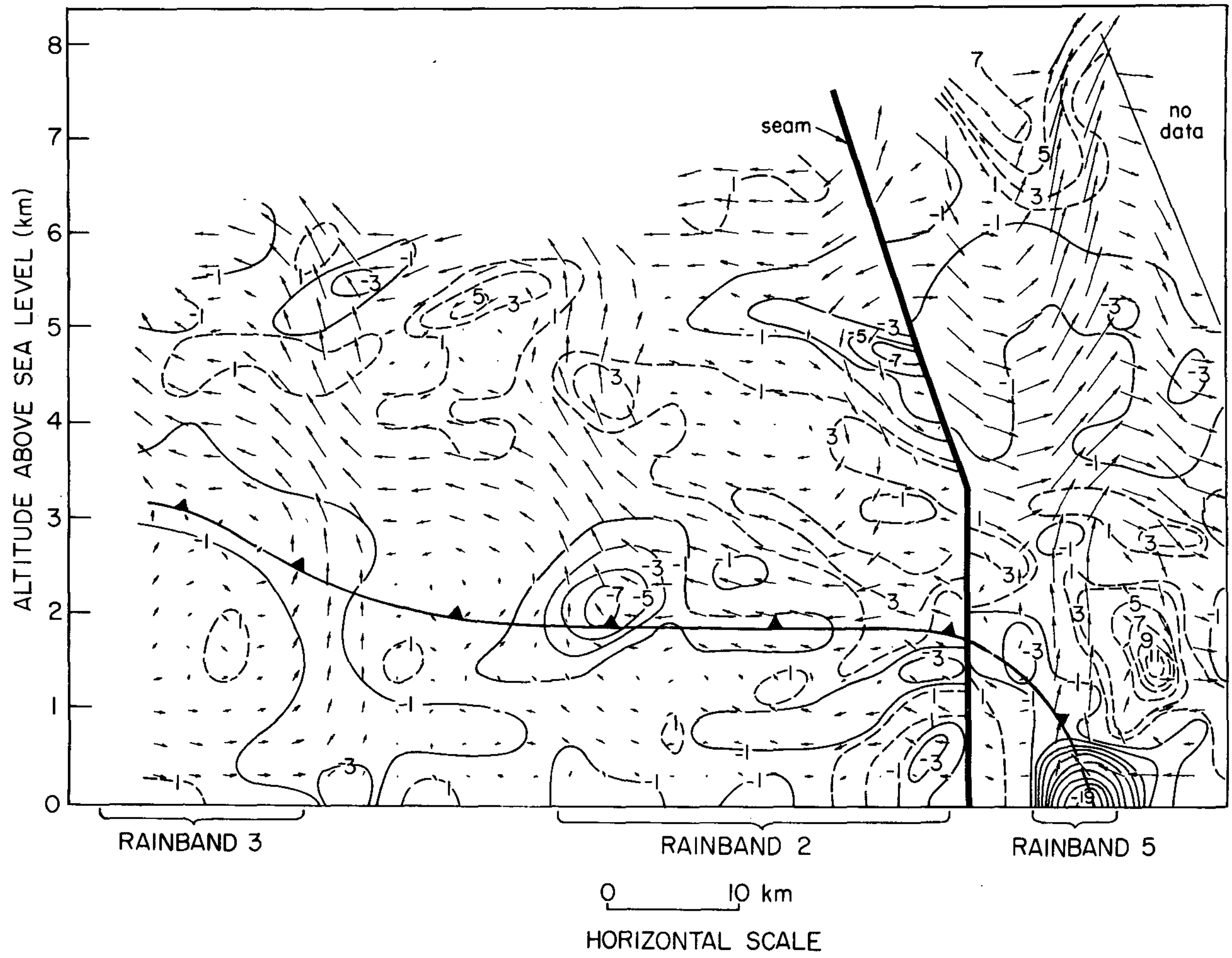

FIG. 14. Cross section through the wide cold-frontal (2 and 3) and the narrow cold-frontal (5) rainbands showing the streamflow *relative to the cold front* and the narrow cold-frontal rainband. The arrows represent 5 min displacements. The continuous lines show the calculated cross-front convergence and the dashed lines the calculated divergence (10^{-4} s^{-1}). To the right of the seam the computations are for 0700 PST, to the left for 0730 PST. The motion of the front and rainbands are toward the right. Vertical wind shear data from the CP-3 radar showed that the cold front was located at the top of the layer of cold advection.

net rate of condensation in the volume to be relatively insensitive to conditions in this region as well as to the exact placement of the upper boundary of the volume. The positioning of the lateral boundaries of the volume in which condensation was occurring was more difficult. In general, these edges were fixed so that the core of largest vertical motions associated with the rainband was enclosed and the width of the volume in the cross section was roughly the same as the width of the band of precipitation at the ground.

Fig. 17 shows the rates of condensation in the warm-sector rainband. Fig. 17 should be compared with Fig. 12, which shows the corresponding streamflow and convergence-divergence fields. The greatest condensation in the warm-sector rainband occurred below ~4 km.

The radar reflectivities in the warm-sector subband (a) indicated the presence of precipitation to above 6 km; however, above 4 km the reflectivity values were very low. Hence, the predominant contribution to the mass of precipitation in sub-band (a) occurred in the strong updraft which originated at low levels. The ratio of the precipitation rate from sub-band (a) to the rate of condensation (i.e., the *precipitation efficiency*) in the strong updraft zone was calculated to be ~40%. The core of the precipitation from the warm-sector sub-band (b) occurred below a region of less strong, multiple updrafts. Calculation of the precipitation efficiency for sub-band (b) produced a ratio of precipitation rate to condensation rate of ~70–80%. There are two reasons that may explain the difference between this efficiency and that of the warm-sector sub-band (a). First, at the times the airflows for warm-sector sub-bands (a) and (b) were calculated, sub-band (a) was a vigorous, well-defined line, while sub-band (b), probably an older feature, was becoming pro-

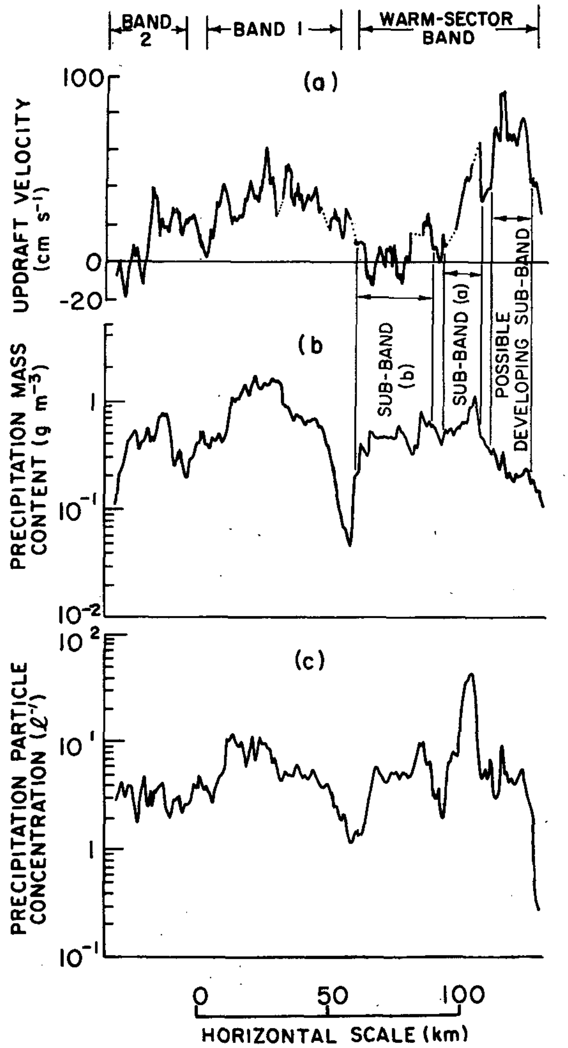

FIG. 15. Airborne measurements obtained during a horizontal traverse at 4.5 km (−9°C) of the warm-sector rainband and wide cold-frontal rainbands. The size range covered by the particle measurements was 0.25–3.12 mm maximum dimensions. Dotted lines are used in (a) where measurements were not obtained.

gressively less well-organized and more difficult to define. It is possible that sub-band (b), while still heavily precipitating, was weakening dynamically. The non-steady-state nature of sub-band (b) at the time the airflow was calculated would therefore lead to an overestimation of its precipitation efficiency. Second, the airflow pattern shown in Fig. 12 and the radar reflectivity data suggest that precipitation carried by the flow rearward from sub-band (a) (toward the left in Fig. 12) contributed to the precipitation that fell into sub-band (b).

Perhaps a more meaningful precipitation efficiency than those calculated for the individual sub-bands is a precipitation efficiency calculated for the entire warm-sector rainband, which consisted of the warm-sector sub-bands (a) and (b), some lighter, trailing precipitation behind (b), and the leading element, which was dynamically active but not yet strongly precipitating, developing ahead of of sub-band (a). This complex of convective elements at various stages of maturity is assumed here to have been reasonably steady state. The precipitation efficiency calculated for the entire warm-sector rainband was ~40–50%.

Fig. 18, which corresponds to the airflow pattern depicted in Fig. 13, shows condensation rates associated with the wide cold-frontal rainband 1. Relatively weak lifting in the low layer and stronger ascent aloft produced a fairly homogeneous condensation rate through more than 6 km of altitude. The precipitation efficiency of this rainband was calculated to have been at least 80%. This high efficiency indicates a quantitative difference between the precipitation processes in this wide cold-frontal rainband and the strongly convective, more vigorous but less efficient, warm-sector rainband. In the case of the wide cold-frontal rainband, the production of ice crystals in the ascending air aloft led to the formation of precipitation particles and the efficient consumption of condensate in the main region of uplift, which occurred at temperatures below 0°C (see Section 3f).

The condensation rates in the narrow cold-frontal rainband 5 and the wide cold-frontal rainbands 2 and 3 are shown in Fig. 19, which corresponds to the airflow pattern of Fig. 14. High condensation rates occur in the narrow updraft associated with the narrow cold-frontal rainband, and broader regions of lower condensation rates occur above the cold front, roughly above the two wide cold-frontal rainbands at the ground.

The precipitation efficiency in the narrow cold-frontal rainband was calculated to be ~30–50% when only condensation in the updraft, up to the strong shear layer at 3.5 km, was considered. As discussed in Section 3d, vertical velocities above this layer are less reliable; the inclusion of the condensation rates associated with them lowers the precipitation efficiency to between ~20–30%. The ratio of the precipitation rate to the strong boundary layer *vapor flux* in the narrow updraft that fed the narrow cold-frontal rainband (Fig. 14) was calculated to be ~20–30%.

The calculation of precipitation efficiencies for the wide cold-frontal rainband 2 was not attempted due to the ill-defined nature of this rainband and the high degree of inhomogeneity along its length.

The precipitation efficiency of wide cold-frontal rainband 3 was calculated to be ~20%. Precipitation in this rainband developed in air that was lifted above the cold front and fell through the cold air mass; radar reflectivity data indicate that some evaporation of this precipitation was occurring. This evaporation may account for the very low precipita-

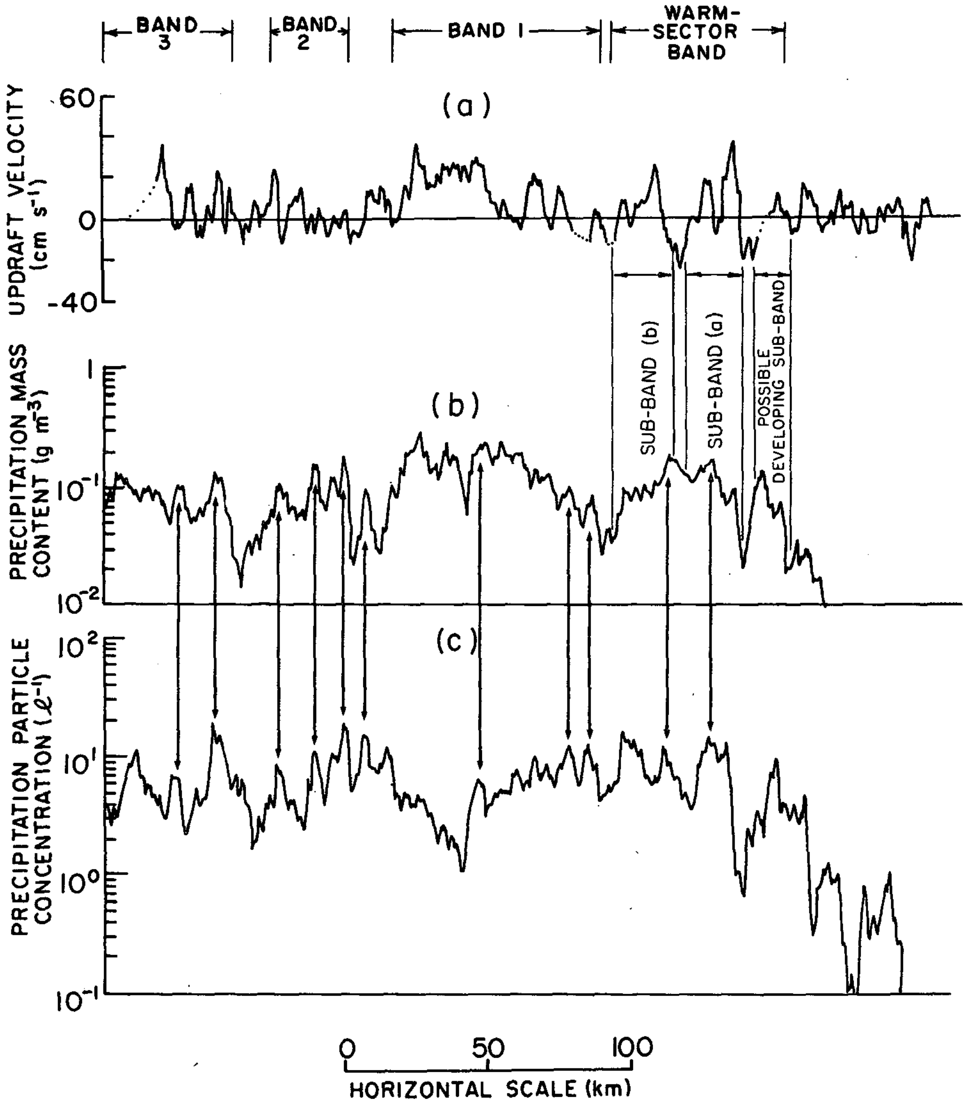

Fig. 16. As in Fig., 15 except at an altitude of 6.4 km (−20°C).

tion efficiency of this rainband. The evaporation of precipitation falling from the upper level cloud decks behind cold fronts can often be observed visually as virga.

Table 6 summarizes the results of our calculations of the precipitation efficiencies of the rainbands.

f. Microphysical characteristics of the clouds and precipitation

Detailed information on the microstructures of the clouds and precipitation associated with the cold front were obtained from the B-23 and Sabreliner aircraft, which flew a series of horizontal passes through the rainbands at various altitudes between 2.1 and 6.4 km. The results of these measurements are described below.

1) General microphysical structure of the precipitation zone aloft

Above the 0°C level (3 km altitude), the precipitation observed both inside and outside the rainbands was in the form of ice particles. Between the 0 and −15°C (5.5 km altitude) levels, the precipitation consisted mainly of aggregates of columns, stellars, dendrites, needles and irregular ice particles. Between the −15 and −20°C levels, aggregation was slightly less pronounced, and columns, platelike crystals, bullet rosettes and aggregates of columns and bullets were found. Above the −20°C level, aggregation among these particles types decreased markedly.

Although the relative humidity was generally close to 100%, liquid water was usually very scarce throughout the region above the 0°C level—occa-

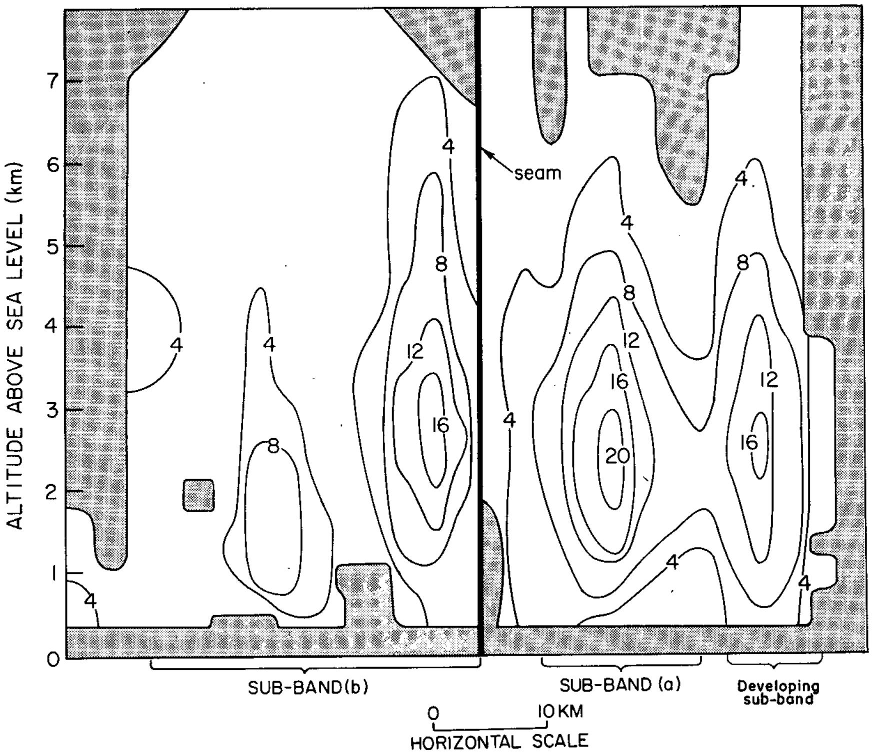

FIG. 17. Calculated condensation rates (10^{-7} kg s^{-1} m^{-3}) shown in a vertical plane oriented perpendicular to the width of the warm-sector rainband. Shaded areas indicate either regions below cloud base or regions of no updraft. To the right of the seam the computations are for 0530 PST, to the left for 0600 PST. (Compare with Fig. 12).

sional patches of cloud liquid water, in amounts between 0.1 and 0.2 g m^{-3}, were observed within ~1 km above the 0°C level in the clouds associated with the wide cold-frontal rainbands. These patches apparently were due to the lifting above 4 km altitude in the wide cold-frontal rainbands (see Figs. 13 and 14). A deeper region of cloud liquid water, in amounts between 0.1 and 0.4 g m^{-3}, was associated with the deep convective updrafts in the new leading elements of the warm-sector sub-band (a) and the developing sub-band ahead of it.

Below 6 km in altitude, the microphysical structures of the rainbands differed significantly from those of the surrounding stratiform clouds in which they were embedded. Fig. 16b shows that the precipitation mass contents[6] at the −20°C (6.4 km altitude) level were typically 2–4 times higher in the rainbands than in the regions between the bands. The particle concentrations in the rainbands below 6 km were higher than those between the bands, and ranged from ~2 to 40 ℓ^{-1} (see Fig. 15c). In the region above ~6 km, however, where precipitation in the bands was only weakly developed, the particle concentrations in the rainbands were generally similar to those in the surrounding cloud and fluctuated between ~2 and 20 ℓ^{-1} (see Fig. 16c).

The growth of precipitation in the ice phase within the bands can be seen in the vertical variation of precipitation mass contents, which ranged from ~0.1 g m^{-3} in the region above 6 km (~−18°C) to ~1.2 g m^{-3} at 3.5 km (near the 0°C level). Vertically pointing CP-3 radar measurements indicate that precipitation was falling in very weak precipitation trails, ~2–10 km across, which originated at levels above 6 km (there was a layer of potentially unstable air immediately above the cold front in the wide cold-frontal rainbands—see Fig. 4). In the wide cold-frontal rainbands, these trails were visible on the CP-3 radar down to the 0°C level. In the warm-sector rainband, the trails were obscured at middle levels by stronger precipitation shafts associated with deep convection from below. The airborne measurements at 6.4 km (−20°C) in these bands reflect the presence of those weak trails through the fluctuations in the precipitation mass content which occur on a horizontal scale of 5–10 km (see Fig. 16b). Correspondence between increases in precipitation mass content and particle concentration (highlighted by the arrows in Fig. 16) indicates that the particle concentrations in the trails were frequently higher than those in the surrounding precipitation. Aircraft measurements at 4.5 km (see Fig. 15) show less

---

[6] Estimates of the precipitation mass contents were derived from the measured particle size spectra by assigning to each particle group an approximate bulk density to convert measured particle diameter into mass. The bulk densities, which were based on Knollenberg's (1975) measurements, ranged from 0.2 g cm^{-3} for particles 0.25 mm in diameter to 0.06 g cm^{-3} for particles 3.2 mm in diameter.

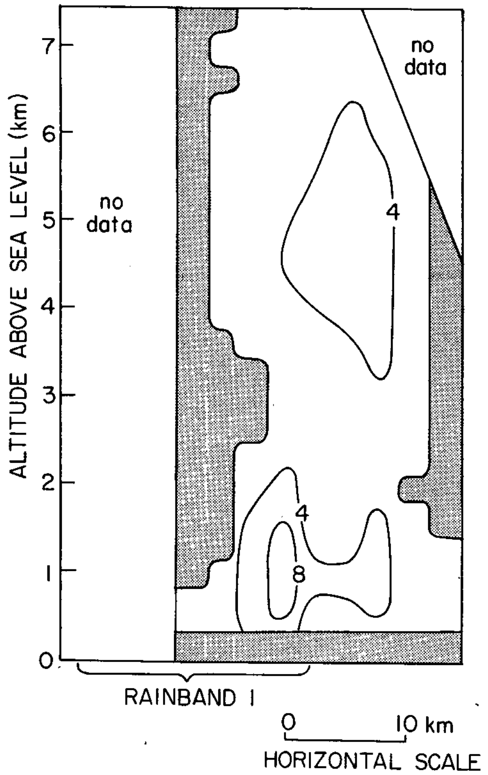

FIG. 18. Calculated condensation rates (10^{-7} kg s^{-1} m^{-3}) shown in a vertical plane oriented perpendicular to the width of the wide cold-frontal rainband 1. Shaded areas indicate either regions below cloud base or regions of no updraft. Computations are for 0630 PST. (Compare with Fig. 13).

evidence of embedded precipitation trails; this was apparently due to the trails spreading and merging with the surrounding precipitation at lower altitudes.

TABLE 6. Precipitation efficiencies in the rainbands.

	Total precipitation rate (kg s^{-1}) in a strip 1 m in width perpendicular to the rainband	Total condensation rate (kg s^{-1}) in a strip 1 m in width perpendicular to the rainband	Precipitation efficiency (%)
Warm-sector rainband*	100–123	244	40–50
Wide cold-frontal rainband 1	40–50	52	80–100
Wide cold-frontal rainband 3	6	27	20
Narrow cold-frontal rainband 5	11–18	33**	30–50

* Includes sub-bands (a) and (b), the leading, developing sub-band, and light trailing precipitation associated with the warm-sector rainband.

** Updraft is assumed to extend to an altitude of 3.5 km.

2) VERTICAL PROFILES OF PRECIPITATION PARTICLE CONCENTRATIONS IN THE RAINBANDS

The differences in dynamics between the warm-sector and wide cold-frontal rainbands resulted in differences in the microstructures of the bands, especially below the −15°C level (5.5 km altitude). In the warm-sector band (Fig. 20a), the average particle concentrations remained nearly constant with decreasing altitude, whereas in the wide cold-frontal bands 1 and 2 the concentrations decreased with decreasing altitude (Fig. 20b). In both types of bands, these trends were due mainly to changes in the concentrations of particles $\leq$ 1.5 mm in diameter.

Evaporation was not occurring between the 0 and

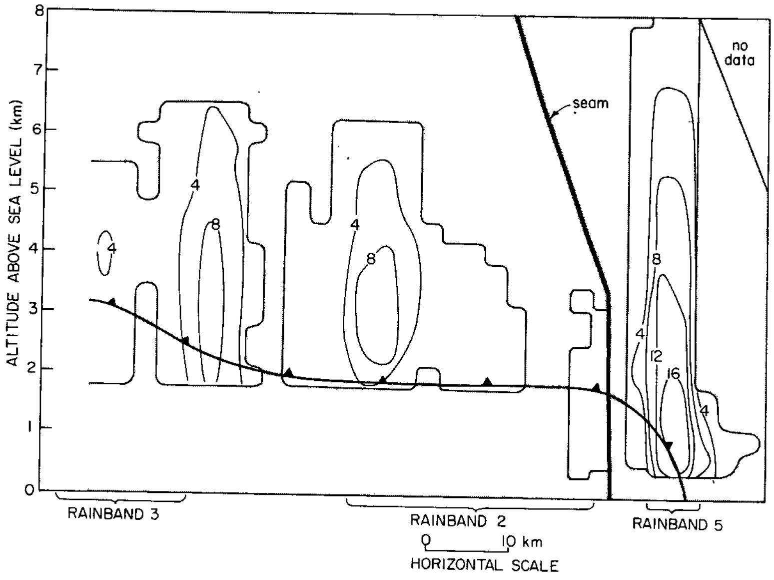

FIG. 19. Calculated condensation rates (10^{-7} kg s^{-1} m^{-3}) shown in a vertical plane oriented perpendicular to the cold front, the narrow cold-frontal rainband 5 and the wide cold-frontal rainbands 2 and 3. Shaded areas indicate either regions below cloud base or regions of no updraft. To the right of the seam the computations are for 0700 PST, to the left for 0730 PST. (Compare with Fig. 14).

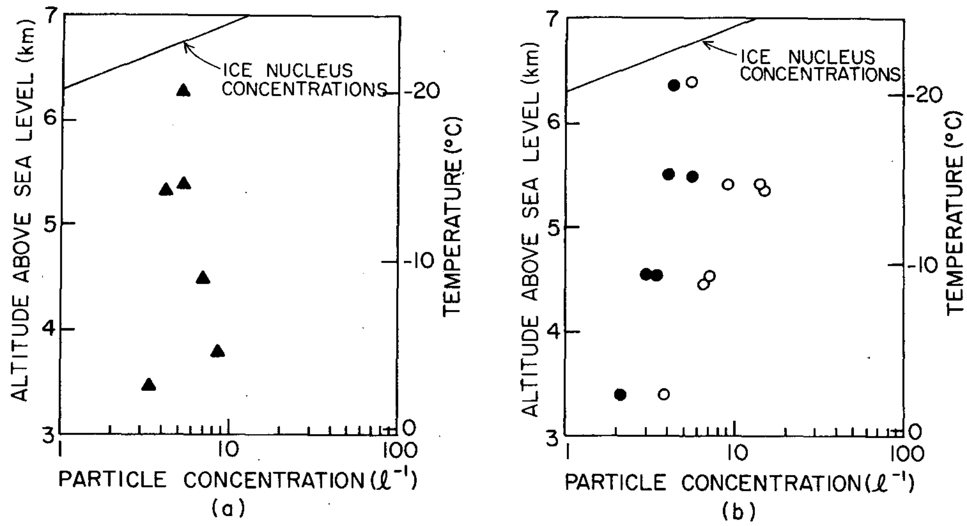

FIG. 20. Vertical profiles of average precipitation particle (0.25–3.12 mm) concentrations in (a) the warm-sector rainband and (b) two wide cold-frontal rainbands (rainband 1, circles; rainband 2, black dots). The solid line at the top of each diagram indicates typical ice nucleus concentrations.

−20°C levels (3–6.2 km altitude) in the wide cold-frontal rainbands represented in Fig. 20b. Therefore, the decreases in average particle concentrations with decreasing altitude that were observed in these rainbands must have been due to aggregation of the falling ice particles, which was observed in the rainbands between the 0 and −20°C levels. Prominent aggregation, however, was also observed in the region below the −20°C level (6.2 km altitude) in the warm-sector band, where the average ice particle concentrations did not decrease with decreasing altitude. This suggests that the strong updrafts observed below 4.5 km altitude in the warm-sector rainband caused new ice particles to form and, perhaps, to be suspended at these lower levels, thereby offsetting the diminution of average particle concentration due to aggregation. The mechanisms that might have led to the formation of new particles are discussed below.

3) ORIGINS OF THE ICE PARTICLES IN THE RAINBANDS

The region above the −15°C level (5.5 km altitude) was an important source of small (0.23–1 mm) precipitation particles in both the warm-sector and the wide cold-frontal rainbands. Particle size spectra at the 6.4 km level (−20°C) show significantly higher concentrations of these small precipitation particles than at lower levels. Hence, these particles must have originated at temperatures close to −20°C. The radar and airborne observations of precipitation trails suggest that 30–60% of the mass of precipitation originating near the −20°C level in both the warm-sector and the wide cold-frontal rainbands formed in upper level cellular convection triggered by potential instability. As can be seen in Fig. 20, the concentrations of ice nuclei active in the tops of the clouds associated with the rainbands should have been sufficient to account for a significant fraction of the particle number concentrations that were measured in the bands.

The deep convective activity in the warm-sector sub-band (a) and the developing sub-band (see Fig. 12) seemed to provide an important, low-level source of small precipitation particles. This is illustrated in the measurements shown in Fig. 15, which show that a sharp peak in particle concentrations was located immediately behind the region of peak updrafts associated with sub-bands (a) and the developing sub-band. Furthermore, the particle-size spectra shown in Fig. 21 indicate that the concentrations of small particles in the convection associated with sub-band (a) and the developing sub-band were significantly higher than those in the stratiform precipitation toward the rear sub-band (b). Additional penetrations below the −15°C level confirmed this pattern.

Since the concentrations of ice nuclei active at temperatures above −15°C are usually $< 0.1\ \ell^{-1}$, it is doubtful that a significant portion of the high particle concentrations observed at low levels in the warm-sector band was due to the activation of ice nuclei at low levels. Nevertheless, most of the particles between 0.25 and 1 mm in diameter in this region of the band were ice. Some of these particles could have been produced by the fragmentation of delicate ice crystals (Hobbs and Farber, 1972; Vardiman, 1978), especially on the flanks of the main updraft regions where large ice aggregates from above would have been subjected to strong turbulence. Small crystal fragments and irregular crystal

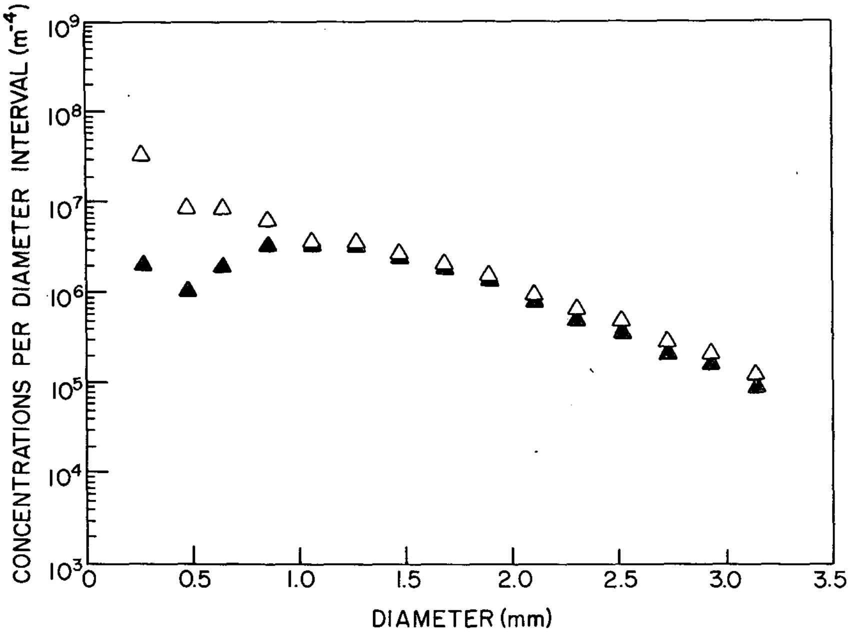

FIG. 21. Particle-size spectra in the convection associated with warm-sector sub-band (a) and the developing sub-band (unshaded triangles) and the stratiform region of warm-sector sub-band (b) (shaded triangles) at 4.5 km altitude (−9°C).

forms, which may have been derived from fragments, were common in the warm-sector band. The production of ice splinters during riming at temperatures between −3 to −8°C (Hallet and Mossop, 1974) could also have provided a low-level source of small ice particles, especially near the centers of the updrafts where cloud liquid water and heavy riming were observed. The relatively low concentrations of ice particles measured in the updraft cores suggest that any ice splinters produced there were probably carried outside the cores before they grew to detectable sizes (~0.2 mm diameter). The freezing of drops, carried upward through the 0°C level, probably contributed slightly to the ice particle concentrations observed in the convective portion of the warm-sector band, since a small number of frozen drops were observed in this region. Frozen drops were not observed in any of the other rainbands.

The wide cold-frontal rainbands generally lacked strong low-level updrafts and supercooled liquid water, suggesting that processes such as droplet freezing and the ejection of ice splinters during riming were unimportant at low levels in these bands.

4) GROWTH OF PRECIPITATION IN THE RAINBANDS

In this section we will show that the "seeder-feeder" cloud process, first proposed by Bergeron (1950) for precipitation growth in orographic clouds, played an important role in the formation of precipitation in the wide cold-frontal rainbands and in portions of the warm-sector rainband.

The fractions of the total masses of precipitation that were produced in various regions of the wide cold-frontal rainbands are indicated schematically in Fig. 22. These fractions were estimated from airborne particle measurements, such as those shown in Figs. 15b and 16b, in combination with measurements of the radar reflectivity factors in the bands. The "seeder" zone, located above the −15°C level in the wide cold-frontal rainband (Fig. 22), consisted of weak convective generating cells embedded in heavy cirrostratus cloud. The predominance of

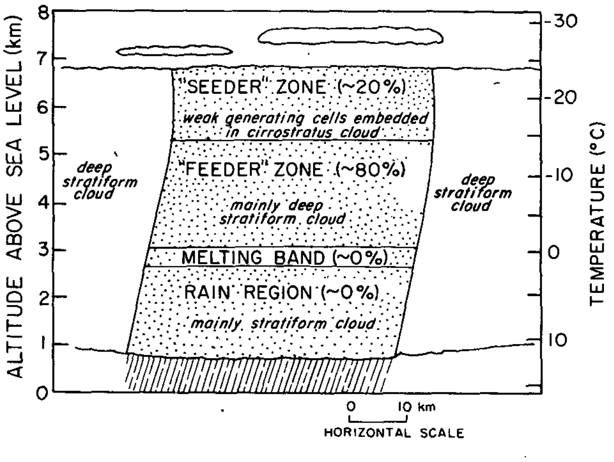

FIG. 22. Schematic cross section of the wide cold-frontal rainbands (shaded) showing approximate fractions of the total mass of the precipitation which were produced in various regions of the band.

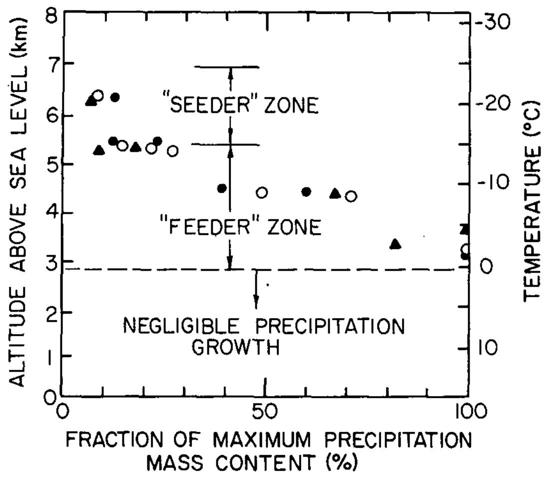

FIG. 23. Normalized vertical profiles of precipitation mass content averaged across the widths of two wide cold-frontal rainbands (rainband 1, unshaded circles; rainband 2, shaded circles) and the warm-sector rainband (triangles).

single, relatively pristine crystals indicated that vapor deposition was the primary growth mode in the cirrostratus cloud, although some aggregation was also observed. Larger particles showing higher degrees of aggregation and some riming were associated with the embedded generating cells, where liquid water was occasionally observed. The measurements shown in Fig. 23 indicate that the particle growth that took place in the "seeder" zone resulted in average precipitation mass contents at the base[7] of this region (5.3 km altitude) which were ~20% of the maximum average mass contents observed just above the 0°C level in the rainbands. The remaining 80% of the precipitation mass was produced in the "feeder" zone, which consisted of a broad area of stratiform cloud and precipitation located roughly between the −15 and 0°C levels. The large, generally unrimed flakes observed in this zone indicate that large precipitation particles there were formed mainly through the aggregation of smaller particles. The role of vapor deposition in the growth of precipitation in the "feeder" zone is examined below.

The sharp increase in precipitation mass content with decreasing height observed in the "feeder" zone (Fig. 23) could have been produced by two processes: vapor deposition within the "feeder" zone, and horizontal advection of particles into this zone as the bands overtook regions of cloud and light precipitation at low levels. In order to determine which of these processes was dominant, estimates of the total rate of mass growth by deposition of vapor onto particles in the rainbands were made by dividing the "feeder" zone into eight layers each 0.31 km in depth. The average particle-size spectrum in each layer was provided by the airborne particle spectrum measurements. The rate of depositional growth (dM/dt) in each layer was then determined from

$$\frac{dM}{dt} = S_i \sum_{\mathrm{I}=1}^{15} N(\mathrm{I})C(\mathrm{I})F^*(\mathrm{I})G(T,P), \qquad (1)$$

where S_i is the supersaturation with respect to ice, $N(\mathrm{I})$ the concentration of ice particles in size group I, $C(\mathrm{I})$ and $F^*(\mathrm{I})$ are shape and ventilation factors, respectively, for the particles in size group I, and $G(T,P)$ is a heat flux factor given by Mason (1971). The total rate of depositional growth in the "feeder" zone was obtained by summing the deposition rates given by (1) over all eight layers of that zone.

The calculated total depositional growth rates for the "feeder" zone are compared with the measured rates of precipitation production in Table 7. The difference between the precipitation rates at the top and the bottom of this zone represents the rate of precipitation production in the "feeder" zone; this is shown in the third column of Table 7. The fourth column shows that for relative humidities between ~96 and 98%, the total rates of depositional growth calculated from (1) were approximately equal to the observed rates of precipitation production in the "feeder" zone of the two wide cold-frontal rainbands. Since the relative humidities measured in this region were within the 92–98% range, it appears quite likely that depositional growth in the "feeder" zone of the wide cold-frontal bands accounted for 90% or more of the mass of ice required to sustain the precipitation production observed in this zone. This fraction represents ~72% of the total amount of precipitation produced by the wide cold-frontal rainbands. Estimates of the net horizontal advection of precipitation into the "feeder" zone of the rainbands ranged from ~0.01 to 0.1 g m^{-2} s^{-1}, indicating that horizontal advection could have supplied only about 10% or less of the mass of ice required to sustain the precipitation growth observed in the "feeder" zone.

The growth of precipitation in the warm-sector rainband is summarized in Fig. 24, which is based on radar and aircraft observations. Both the "seeder-feeder" process and deep convection played a role in the production of precipitation in this band. As in the wide cold-frontal bands, the top of the warm-sector band functioned as a "seeder" zone. This zone consisted of heavy cirrostratus cloud containing light precipitation and a few weak generating cells. Particle aggregation and riming in the cirrostratus cloud were generally slight, suggesting that particle growth by vapor deposition was crucial in this region. The airborne measurements shown in Fig. 23 indicate that 10–20% of the mass of the precipitation in the warm-sector rainband originated

---

[7] The boundary between the "seeder" and "feeder" zones corresponds to the base of the upper level convection.

TABLE 7. Observed and calculated rates of precipitation production in the "feeder" zone of the wide cold-frontal rainbands 1 and 2.

	Observed precipitation rate [g m^{-2} s^{-1} (mm h^{-1})] at top of "feeder" zone	Observed precipitation rate [g m^{-2} s^{-1} (mm h^{-1})] at bottom of "feeder" zone	Observed rate of precipitation production (g m^{-2} s^{-1}) in the "feeder" zone	Calculated total rate of deposition (g m^{-2} s^{-1}) in the "feeder" zone at relative humidities of				
				92%	94%	96%	98%	100%
Wide cold-frontal rainband 1	0.4 (1.4)	1.7 (6.2)	1.3	0.5	0.7	1.0	1.4	1.9
Wide cold-frontal rainband 2	0.3 (1.1)	1.1 (4.1)	0.8	0.3	0.4	0.6	0.9	1.3

in the "seeder" zone above 5.4 km altitude. The remaining 80–90% of the precipitation growth occurred in two distinct regions below this level. One of these regions was a zone of deep, vigorous convection which contained the developing sub-band and sub-band (a). Radar reflectivity factor measurements, as well as airborne measurements such as those shown in Fig. 15, indicate that 50–60% of the mass of the precipitation in the main warm-sector rainband developed in this zone of deep convection. The convection here produced a region of water-saturated cloud in which precipitation particles grew by riming, deposition and aggregation. The high degrees of riming commonly observed on the large precipitation particles in this region emphasize the important role played by the "seeder" zone, which introduced solid precipitation particles into the tops of the convection, assuring rapid precipitation growth through mixed-phase processes. The airflow in Fig. 12 suggests that some moisture in the convective updrafts in the warm-sector sub-band (a) flowed rearward into sub-band (b). This mid-level flow helped to produce a stratiform "feeder" zone in the rear portion of sub-band (b) in which "seed" particles falling from above grew by deposition and aggregation. Weak stratiform updrafts in this "feeder" zone may have supplemented the moisture available for precipitation growth in this region, which accounted for ~30–40% of the total mass of precipitation in the warm-sector rainband.

4. Summary

The clouds and precipitation preceding and accompanying a cold front have been described in detail. The mesoscale organization of the clouds and precipitation into a series of rainbands was observed, and analyses of the mesoscale airflows associated with the rainbands and of the microphysical characteristics of the clouds at different altitudes have enabled several aspects of the cloud dynamics and the growth of precipitation in the mesoscale rainbands to be elucidated.

A schematic depiction of the general cloud structure associated with this cold-frontal system, the mesoscale organization of the precipitation, and some of the characteristics and internal features of these rainbands are shown in Fig. 25. The principal results of this case study may be summarized as follows:

- The regions of heaviest precipitation were organized into six mesoscale bands of precipitation, all oriented parallel or nearly parallel to the cold front. They were a warm-sector band (situated ahead of the cold front), a narrow cold-frontal band and four wide cold-frontal bands.
- The warm-sector rainband consisted of a series of mesoscale, convective sub-bands. One sub-band formed near the surface cold front, and two additional sub-bands formed ahead of it. These sub-bands all advanced relative to the cold front. Air at low levels ahead of the sub-bands ascended rapidly in the sub-bands and flowed to the rear of the sub-bands in the middle troposphere. Updrafts were stronger and precipitation particle populations were younger in the leading convective sub-bands. In the rear sub-band, the airflow was weaker and less organized, and the precipitation particle populations were older. In these respects, the sub-bands con-

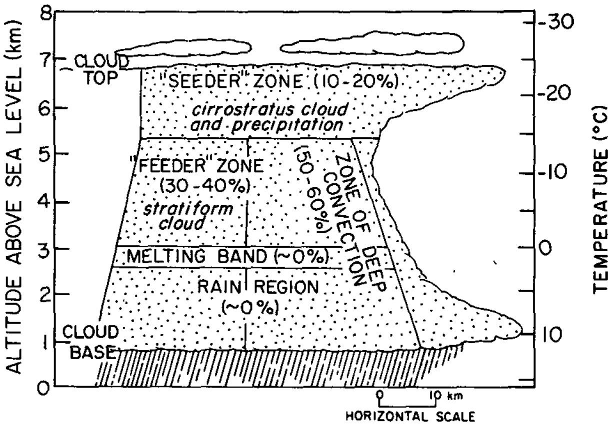

FIG. 24. Schematic cross section of the warm-sector rainband showing approximate fractions of the total mass of the precipitation which was produced in various regions of the band.

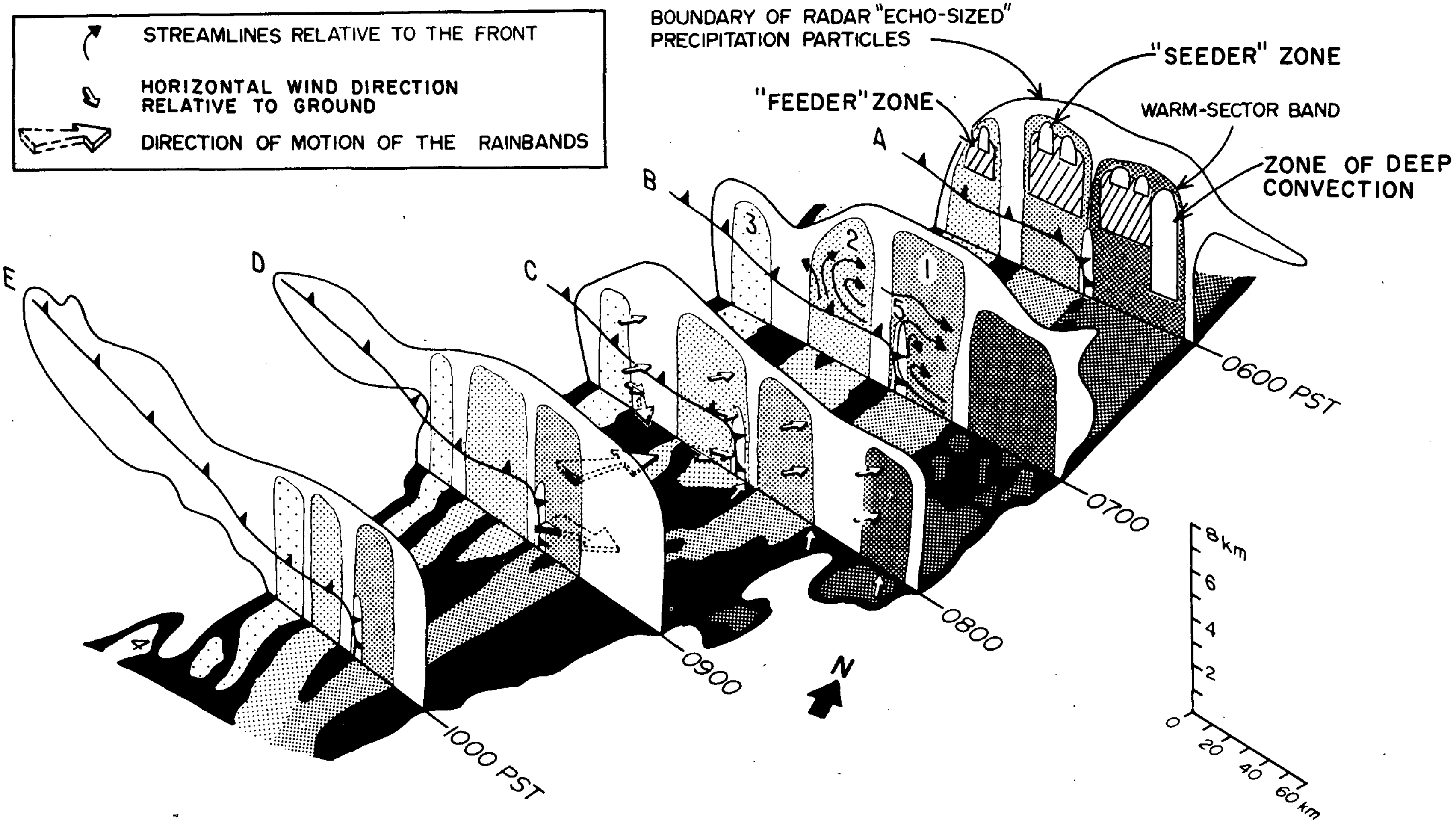

FIG. 25. A schematic summary of the structure and organization of the clouds and precipitation and air flow associated with the cold front described in this paper. The outline of the radar echo pattern in a vertical plane normal to the front is shown for five different times. The various rainbands (1–5 and the warm-frontal band) discussed in this paper are indicated by different shadings. Various features of the structure are highlighted in each vertical section. Shown in A are locations of "feeder-seeder" zones and the regions of deeper convection, in B the streamlines of the airflow relative to the front, in C the horizontal winds, and in D the motions of the wide and narrow cold-frontal rainbands.

stituting the warm-sector rainband resembled the lines of convection in much stronger, propagating squall lines.

- The narrow cold-frontal rainband, which coincided and moved with the surface front, originated in low-level convection at the cold front. The convection was a consequence of strong horizontal convergence of air in the boundary layer of a southerly jet of warm, moist air ahead of the cold front. The convergence near the ground within the narrow cold-frontal rainband was $\sim 1.9 \times 10^{-3}$ s^{-1}, and the air in this region rose sharply with a vertical velocity of ~ 1 m s^{-1} in a column ~ 5 km wide. This updraft, apparently coupled with a downdraft just ahead of the front, was probably responsible for the organization of heavy precipitation on the front into small mesoscale, ellipsoidal areas with similar orientations.
- The wide cold-frontal rainbands were associated with ascending air at altitudes above 3 km. These bands originated above the cold-frontal surface, behind the position of the surface front, and advanced faster than the front itself. One of the wide cold-frontal rainbands was observed to advance from behind the surface front and the narrow cold-frontal rainband to a position immediately ahead of them. Such relative motions reflect the fact that the wide and narrow cold-frontal rainbands were associated with air motions organized at different altitudes.
- Cumulus-scale and small mesoscale cores of intense precipitation embedded within the larger mesoscale wide cold-frontal rainbands moved with the winds at upper levels, in the region of ascent. Precipitation cores in the warm-sector rainband moved with both the winds in the low-level jet and the winds at upper levels, which were nearly identical. The motions of the rainbands themselves were similar to the motions of the precipitation cores comprising them.
- The precipitation efficiency (precipitation rate/condensation rate) in the warm-sector rainband was ~40–50%. The precipitation efficiency in the narrow cold-frontal rainband was ~30–50%. (The ratio of the precipitation rate to the vapor flux of boundary layer air entering the updraft of the narrow cold-frontal rainband was ~20–30%.) One of the wide cold-frontal rainbands, in which there was a steady production of ice particles in the main region of uplift, had a precipitation efficiency of at least 80%. Another wide cold-frontal rainband, in which some of the precipitation evaporated before reaching the ground, had a precipitation efficiency of ~20%.
- An important source of precipitable particles in the wide cold-frontal rainbands occurred at high levels, in shallow convective cells aloft (the "seeder" zone). Ice particles, which grew largely by deposition at the high levels, fell through lower level clouds (the "feeder" zone) where they grew by aggregation and deposition. About 20% of the mass of precipitation in these bands originated in the "seeder" zones and ~80% in the "feeder" zones.
- "Seeder-feeder" zones also played a role in the production of precipitation in the warm-sector rainband. In the deep, vigorous convection occurring toward the leading portion of this band, heavy riming and aggregation were important in the growth of precipitable particles.

Acknowledgments. Thanks are due to all members of the University of Washington's Cloud Physics Group and to personnel from the National Center for Atmospheric Research's (NCAR) Atmospheric Technology Division for their valuable contributions to this study. The CYCLES PROJECT is supported by the Experimental Meteorology and Weather Modification Program, Division of Atmospheric Sciences, National Science Foundation (NSF) under Grants ATM74-14726-A02 and ATM77-01344, the Air Force Office of Scientific Research (Contract F49620-77-C-0057), the Environmental Research Laboratories of the National Oceanic and Atmospheric Administration (Grants 04-7023 and 44033), and the U.S. Army Research Office (DAAG 29-79-G-0005). The CP-3 radar and Sabreliner aircraft were provided by NCAR, which is sponsored by NSF.

REFERENCES

Austin, P. M., and R. A. Houze, Jr., 1972: Analysis of the structure of precipitation patterns in New England. *J. Appl. Meteor.*, **11**, 926–935.

Baynton, H. W., J. Serafin, C. L. Frush, G. R. Gray, P. V. Hobbs, R. A. Houze, Jr. and J. D. Locatelli, 1977: Real-time wind measurements in extratropical cyclones by means of Doppler radar. *J. Appl. Meteor.*, **16**, 1022–1028.

Bergeron, T., 1950: Über der mechanisms der ausgiebigen Nederschläge. *Ber. Dtsch. Wetterd.*, **12**, 225–232.

Browning, K. A., and T. W. Harrold, 1969: Air motion and precipitation growth in a wave depression. *Quart. J. Roy. Meteor. Soc.*, **95**, 288–309.

——, and C. W. Pardoe, 1973: Structure of low-level jet streams ahead of midlatitude cold fronts. *Quart. J. Roy. Meteor. Soc.*, **99**, 619–638.

Elliott, R. D., and E. L. Hovind, 1964: On convection bands within Pacific coast storms and their relation to storm structure. *J. Appl. Meteor.*, **3**, 143–154.

Hallett, J., and S. C. Mossop, 1974: Production of secondary ice particles during the riming process. *Nature*, **249**, 26–28.

Herzegh, P. H., and P. V. Hobbs, 1980: The mesoscale and microscale structure of clouds and precipitation in midlatitude cyclones. II: Warm frontal clouds. *J. Atmos. Sci.*, **37**, 597–611.

Hobbs, P. V., 1978: Organization and structure of clouds and precipitation on the mesoscale and microscale in cyclonic storms. *Rev. Geophys. Space Phys.*, **16**, 741–755.

——, and R. J. Farber, 1972: Fragmentation of ice particles in clouds. *J. Rech. Atmos.*, **6**, 245–258.

——, and J. D. Locatelli, 1978: Rainbands, precipitation cores and generating cells in a cyclonic storm. *J. Atmos. Sci.*, **35**, 230–241.

——, and K. R. Biswas, 1979: The cellular structure of narrow cold-frontal rainbands. *Quart. J. Roy. Meteor. Soc.*, **105,** 723–727.

——, R. A. Houze, Jr. and T. J. Matejka, 1975: The dynamical and microphysical structure of an occluded frontal system and its modification by orography. *J. Atmos. Sci.*, **32,** 1543–1562.

Houze, R. A., Jr., 1977: Structure and dynamics of a tropical squall-line system. *Mon. Wea. Rev.*, **105,** 1540–1567.

——, P. V. Hobbs, K. R. Biswas and W. M. Davis, 1976a: Mesoscale rainbands in extratropical cyclones. *Mon. Wea. Rev.*, **104,** 868–878.

——, J. D. Locatelli and P. V. Hobbs, 1976b: Dynamics and cloud microphysics of the rainbands in an occluded frontal system. *J. Atmos. Sci.*, **33,** 1921–1931.

Knollenberg, R. G., 1975: The response of optical array spectrometers to ice and snow: a study of probe size to crystal mass relationships. Sci. Rep. No. 1, SCI 75C0141-9875-001, ARCRL, Hanscom AFB, MA, 70 pp. [NTIS AD A020276/26A].

Kreitzberg, C. W., 1964: The structure of occlusions as determined from serial ascents and vertically-directed radar. Rep. AFCRL-64-26, 121 pp. [NTIS No. AD-432007.]

Locatelli, J. D., and P. V. Hobbs, 1978: A technique for obtaining detailed wind fields in a frontal system from a single Doppler radar. *J. Appl. Meteor.*, **17,** 1076–1079.

Mason, B. J., 1971: *The Physics of Clouds*. Oxford University Press, 671 pp.

Matejka, T. J., R. A. Houze, Jr. and P. V. Hobbs, 1980: Microphysics and dynamics of the clouds associated with mesoscale rainbands in extratropical cyclones. *Quart. J. Roy. Meteor. Soc.*, **106** (in press).

Nagle, R. E., and S. M. Serebreny, 1962: Radar precipitation echo and satellite cloud observations of a maritime cyclone. *J. Appl. Meteor.*, **1,** 279–295.

Vardiman, L., 1978: The generation of secondary ice particles in clouds by crystal-crystal collision. *J. Atmos. Sci.*, **35,** 2168–2180.